



Title	A study on the latitude of a western boundary current extension jet
Author(s)	陶, 泰典
Citation	北海道大学. 博士(環境科学) 乙第6948号
Issue Date	2015-03-25
DOI	10.14943/doctoral.r6948
Doc URL	http://hdl.handle.net/2115/59340
Type	theses (doctoral)
File Information	Yasunori_Sue.pdf



[Instructions for use](#)

**A study on the latitude of a western
boundary current extension jet**

(西岸境界流続流ジェットの形成緯度に関する研究)

by

Yasunori Sue

Graduate School of Environmental Science Hokkaido University

February 2015

Abstract

This thesis investigates the formation of eastward jets extended from western boundary currents, using a simple two-layer quasi-geostrophic (QG) model forced by a wind stress curl consistent with the formation of a subtropical gyre. The dependency of the latitude of the eastward jet on various parameters and on the meridional distribution of the Ekman pumping velocity was investigated. The parameters considered in the present study included the viscous and inertial western boundary layer width, the parameter representing the degree of the partial slip boundary condition, the ratio of the upper to the lower layer depth, and the bottom friction. With the parameters used, two types of stable structures are found in the time mean field. One type of structure represented the ‘prematurely separated jet case’, in which the eastward extension jet was located far south of the northern boundary of the subtropical gyre, as is the Kuroshio Extension; the other type was the ‘gyre boundary jet case’, in which the eastward jet occurred along the northern boundary. The initial condition decides which type of structure would occur. When the prematurely separated jet case occurred the latitude of the eastward jet depended very little on the parameters. In addition, the latitude was determined by the meridional distribution of the Ekman pumping velocity. The eastward extension jet was usually located near the latitude that was half of the maximum value of the Sverdrup streamfunction and satisfied an integral condition derived from the QG potential vorticity equation.

Contents

Abstract	i
1 Introduction	1
1.1 Western Boundary Currents	1
1.2 Previous studies and Purposes of this study	2
1.3 Contents	5
2 Models and Math Foundation	6
2.1 Two-layer quasi-geostrophic model	6
2.2 IDO-CF scheme	10
3 Results	12
3.1 Two typical solutions	12
3.2 Dependance on parameters	15
3.2.1 Dependencies on viscous and inertial boundary layer width	15
3.2.2 Dependence on boundary condition	16
3.2.3 Other parameters	18
3.2.4 The Influence due to Symmetry	20
3.3 Dependence on Meridional Distribution of Ekman Pumping Velocity	20
3.3.1 Setting on Distributions of the Ekman Pumping Velocity	21
3.3.2 Results	21

3.3.3	Integral Condition for Streamfunction in the Western Region . . .	22
4	Conclusions and Remarks	25
	Figures	29
	Tables	51
	Bibliography	55

Chapter 1

Introduction

1.1 Western Boundary Currents

The large scale wind system on the earth, consisting of westerlies in mid-latitude and trade winds in lower latitude, drives upper layer ocean circulations, which are referred to as wind-driven oceanic gyres. The circulations are cyclonic on the polar side of westerlies and anti-cyclonic between the westerlies and trade winds. Wind-driven gyre is roughly divided into two regions. One is the interior region which is in large eastern areas with relatively slow meridional flow; the other is the western boundary region which is narrow region with a strong meridional flow along the shore. The strong flow is referred to as a western boundary current. The wind-driven circulation system can be explained by linear models in which the external forcing and the frictional effect balance with the beta effect, which represents the effect of roundness of the rotating earth, in a homogeneous fluid on flat bottom. The frictional effect is the bottom frictional effect in the Stommel model (Stommel, 1948) and is the lateral frictional effect in the Munk model (Munk, 1950). The examples of the solutions in either model are shown in Fig. 1. In the interior region the frictional term can be neglected and beta term balances with forcing term, which is referred to as the Sverdrup balance. In the western boundary region the western

boundary current separates at certain latitude and forms an eastward western boundary current extension jet, which is represented by the Kuroshio Extension in the North Pacific and the Gulf Stream in the North Atlantic.

These currents transport large amount of heat and have a great deal of influence on the surrounding climate. In mid-latitudes, the heat transport by the ocean account for about 30% to the total transport (Trenberth and Caron, 2001). Understanding the mechanism determining the path and the separation latitude of western boundary currents and the extension jet is a very important issue on oceanography and climatology.

1.2 Previous studies and Purposes of this study

The linear models can roughly explain the structure of the wind-driven gyres. However, the structures of the western boundary current extension jet and around the jet region are quite different with that in real ocean. Until fine-grid eddy-resolving models were available, understanding the separation of western boundary currents and the formation of their eastward extensions was one of the most important subjects in physical oceanography. Prior to the availability of such models, model simulation could not accurately reproduce the western boundary current separation in real oceans, for example, in the case of the separation of the Kuroshio and Gulf Stream. Model western boundary currents showed a tendency to separate far north of the real separation latitude and the separated currents were weaker and broader than reality and flowed eastward along a course near the subtropical/subpolar gyre boundary predicted by the Sverdrup theory (Bryan and Cox, 1972; Takano et al., 1973; Han, 1984). In the 1990s, eddy-resolving models were developed with development in computing power and successfully used to reproduce the Kuroshio and Gulf Stream (Bleck et al., 1995; Smith et al., 2000) and their extensions with inertial recirculation gyres, which suggest the importance of nonlinearity (e.g., Ierley, 1990; Kamenkovich et al., 1995). Development of these numerical models of

ocean circulation was reviewed in detail by McWilliams (1996).

In spite of the success in reproducing western boundary current separation and eastward extensions, the dynamics of western boundary current separation and the maintenance of eastward jets have not been satisfactorily clarified yet. Because the separation latitude of the Kuroshio coincides with that of the southern coast of Japan and the Gulf Stream separates north of Cape Hatteras, the effects of topographic features of the coastal boundary and/or bottom have also been studied (see, e.g., Dengg, 1993; Özgökmen et al., 1997; Marshall and Tansley, 2001). Recently, Nakano et al. (2008) showed, by using an eddy-resolving ocean GCM with no-slip boundary condition, that the model Kuroshio separates around the same latitude and a realistic Kuroshio Extension accompanying the recirculation gyres occurs even when the topography including the Japan Islands is removed. Therefore, the separation of western boundary currents and their eastward extensions can occur even in a rectangular basin (bounded by meridional and zonal coastlines), although the topography must affect the current in real oceans.

A number of studies have been performed to clarify the properties of the circulation structure in a rectangular basin. One of the most insightful study is the work of Haidvogel et al. (1992). They investigated the dependence of the separation latitude on the wall boundary condition using a partial slip boundary condition and biharmonic viscosity. The authors showed that western boundary currents separate far upstream from the gyre boundary predicted by Sverdrup theory (*'premature separation'* in their terminology), when the applied western boundary condition is close to a no-slip condition using a three-layer quasi-geostrophic (QG) model. Although the appropriate specific boundary condition for defining the real western boundary is not clear, shear with opposite sign on the coastal side of the western boundary current to that on the offshore side seems necessary for premature separation to occur in numerical models, as mentioned by Dengg (1993) and Kiss (2002), and the no-slip boundary condition could be regarded as a parameterization necessary to create the shear layer.

Verron and Blayo (1996) investigated the effects of the scheme estimating the vorticity at the no-slip boundary on the separation problem using a three-layer QG model. They showed that the scheme can strongly affect the circulation pattern when the viscous boundary layer is thinner than the grid size. It was also shown that the asymmetry of wind-stress curl affects the separation point (see also Verron and Le Provost, 1991). Dynamical system approaches have also been used to investigate structures of large scale ocean circulation under nonlinear conditions and their dependence on parameters relating to nonlinearity and viscosity. Verron and Jo (1994) investigated the solution types of the circulation and classified them as stable, unstable or intermediate solutions in a broad range of parameters of viscous and inertial boundary layer width. While Ierley and Sheremet (1995) found multiple solutions at the same parameter values in a barotropic single gyre, Cessi and Ierley (1995) studied symmetry breaking caused by the pitchfork bifurcation for a double-gyre circulation. Further increase in nonlinearity causes a Hopf bifurcation which yields periodic solutions (Jiang et al., 1995). Although the asymmetric solutions found in those studies would be related to the problem of the western boundary current separation, the solutions were very different from that with premature separation obtained by Haidvogel et al. (1992) in which the separation occurs in the subtropical and subpolar gyres symmetrically. The difference could partly arise from the differences in the parameter values and also from the model vertical structure; the models used in the above dynamical system approach were barotropic or 1.5-layer models while Haidvogel et al. (1992) used a three-layer model in a more turbulent regime.

Many recent studies have addressed the dynamics and variability of real western boundary currents and their influences on climate, marine ecosystems, etc. Sasaki and Schneider (2011) studied the mechanism of meridional shifts of the Kuroshio extension jet that propagates from east to west. Sugimoto and Hanawa (2012) showed that the Kuroshio path on the southern coast of Japan is correlated with the stability of the Kuroshio extension jet. Frankignoul et al. (2011) studied the influence of the meridional

shifts of the Kuroshio-Oyashio extensions on the atmospheric circulation, and Sasai et al. (2010) studied the effects of variability of Kuroshio extension on the marine ecosystem, for example.

However, it seems that one of the most basic questions still remains unanswered: What are the parameters that govern the pattern of wind-driven circulation in a rectangular basin, and what determines the latitude of the prematurely separated eastward jet? To address these questions, this thesis revisits the problem of separation of a western boundary current and formation of an eastward jet in a two-layer QG model, which is one of the simplest models able to produce a premature separation. Premature separation could also be seen in a barotropic sliced cylinder model in Griffiths and Kiss (1999) and Kiss (2002) with a horizontally uniform surface stress curl and a curved boundary. It will be shown later that two active layers are needed for premature separation to occur in rectangular basin model.

1.3 Contents

After describing the model configuration and the numerical scheme in chapter 2, typical circulation patterns indicated by the present model are shown and the dependence of the latitude of the eastward extension jet on the parameters and external forcing are discussed in chapter 3. In chapter 4, the remainder are reserved for conclusions and remarks.

Chapter 2

Models and Math Foundation

2.1 Two-layer quasi-geostrophic model

A two-layer quasi-geostrophic model on a β -plane is used in this study. The dimensional form of the equations can be written as

$$\frac{\partial q_j}{\partial t} + J(\psi_j, q_j) = (2 - j) \frac{f_0}{H_1} w_e + \nu \nabla^4 \psi_j - (j - 1) r \nabla^2 \psi_j , \quad (2.1)$$

with

$$q_j = \nabla^2 \psi_j - \frac{\rho_0 f_0^2}{\Delta \rho g H_j} (\psi_j - \psi_{3-j}) + \beta y , \quad (2.2)$$

where j is the layer number ($j = 1$ and $j = 2$ denote upper and lower layer, respectively), t is the time, x and y are the eastward and northward coordinates, respectively, J is the Jacobian, ∇ is the horizontal differential operator. ψ_j and q_j are the streamfunction and the potential vorticity in the j th layer, respectively. The term ρ_0 is the mean density and $\Delta \rho$ is the density difference between the two layers, which is assumed to be much smaller than ρ_0 . g is the gravitational acceleration, f_0 and β are the Coriolis frequency and its meridional gradient at the reference latitude, i.e., $f = f_0 + \beta y$. Tables 1 lists the meaning and the definition of the coefficients.

The non-dimensionlization was carried out using meridional length scale of the wind-driven gyre (L), meridional derivative of the Coriolis parameter (β), and Sverdrup velocity (U). The time was scaled by $(\beta L)^{-1}$. Equations (2.1) and (2.2) are rewritten as

$$\frac{\partial q_j}{\partial t} + \frac{1}{\hat{\beta}} J(\psi_j, q_j) = (2-j)w_e + \hat{\nu} \nabla^4 \psi_j - (j-1) \hat{r} \nabla^2 \psi_j, \quad (2.3)$$

with

$$q_j = \nabla^2 \psi_j - F_j (\psi_j - \psi_{3-j}) + \hat{\beta} y \quad (2.4)$$

ψ_j and q_j are non-dimensional value in the following statements. Tables 2 lists the meaning and the definition of the coefficients along with non-dimensional parameters. Although the parameters in (2.3) and (2.4) are $\hat{\beta}$, $\hat{\nu}$, F_j and \hat{r} , the width of the inertial boundary layer divided by the Rossby radius of deformation (R_I), δ_I , that of the viscous boundary layer, δ_M , the ratio of the upper to the lower layer thickness, H_1/H_2 , and F_I whose square root is the meridional length of the model domain divided by the Rossby radius of deformation will be used, instead of $\hat{\beta}$, $\hat{\nu}$ and F_j . In terms of δ_I , δ_M , F_I and H_j , the parameters, $\hat{\beta}$, $\hat{\nu}$ and F_j , can be written as

$$\hat{\beta} = \frac{2F_I}{\delta_I^2}, \quad \hat{\nu} = \frac{\delta_M^3}{F_I^{3/2}}, \quad F_j = F_I \frac{H_{3-j}}{H_1 + H_2}. \quad (2.5)$$

The first term on the right-hand side of Eq. (2.3) represents an external force, where w_e is the Ekman pumping velocity that is proportional to the curl of the wind stress. The Sverdrup balance in (2.3) is

$$\frac{\partial \psi_{Sv}}{\partial x} = w_e,$$

where ψ_{Sv} is the Sverdrup streamfunction and subscript 'Sv' denotes the value estimated by Sverdrup balance, and $w_e(x, y)$ is set to satisfy that the maximum of ψ_{Sv} at the western boundary is unity. That is,

$$[\psi_{Sv}(X_W, y)]_{max} = \left[\int_{X_E}^{X_W} w_e dx \right]_{max} = 1,$$

where X_E and X_W are the x -coordinates of the eastern and western boundaries, respectively; Y_N and Y_S are the the y -coordinates of the northern and southern boundaries in the same way.

The lateral boundary conditions are no-normal flow and partial-slip, that is,

$$\psi_j = 0 , \quad (2.6)$$

and

$$\frac{\partial^2 \psi_j}{\partial \eta^2} = -\alpha F_I^{\frac{1}{2}} \frac{\partial \psi_j}{\partial \eta} , \quad (2.7)$$

where η is the outward coordinate normal to the boundary and α is the partial-slip coefficient normalized by the Rossby radius of deformation. The partial-slip boundary condition is regarded as the free-slip condition at $\alpha = 0$ and the no-slip condition at the limit of $\alpha \rightarrow \infty$. In the present study, the slip boundary condition was used along the southern, northern, and eastern boundaries, and the partial-slip boundary condition was used along the western boundary. In the case with the no-slip condition, α was set to 5.7×10^2 . Although most of the experiments were conducted in the no-slip boundary condition, experiments with various α were also conducted. Based on the above the parameters governing the present model are

$$F_I, \quad \frac{H_1}{H_2}, \quad \delta_I, \quad \delta_M, \quad \hat{r} \quad \text{and} \quad \alpha.$$

In this thesis, the term $F_I^{1/2}$ is set to 45. To examine the dependence of the solution on the basin scale, an experiment in which $F_I^{1/2} = 30$ is conducted and the circulation pattern showed little difference, which suggests that the dependence on F_I is low when the ocean is much larger than the deformation radius.

The Ekman pumping velocity is set to be of the form

$$w_e(x, y) = \begin{cases} \frac{1}{X_E - X_I} \hat{w}_e(y) & \text{for } X_I \leq x \leq X_E \\ 0 & \text{for } X_W < x < X_I \end{cases} , \quad (2.8)$$

where the maximum value of $\hat{w}_e(y)$ is unity. Although $\hat{w}_e = \sin \pi y$ is used most often, other forms of $\hat{w}_e(y)$ was used to demonstrate the dependence of the solution on the wind-stress distribution. In most of the experiments, the author set $X_E = 2$, $X_I = 1$ and $X_W = 0$. In this profile, the western half of the basin was not forced by Ekman pumping. The extended jet meandered vigorously just after separating from the western boundary and the Ekman pumping velocity tends to weaken the eastward jet (as shown later). The above setting made the extended jet longer in the zonal direction and permitted determination of the spatial mean latitude of the extended jet more unambiguously.

Before proceeding to the numerical results, we considered typical values of parameters. The dimensional parameters are listed in Table 1 and the reference value of $H_1 = 1000\text{m}$ and $H_2 = 4000\text{m}$ gave $R_I \simeq 45\text{km}$. Based on the above parameter values, the dimensional meridional basin scale, L , is 2025km , the time scale of damping by reference bottom friction, which is $\hat{\tau} = 10^{-3}$, is 290 days. Because in the North Pacific the north-south extent of the subtropical gyre is approximately $2,500\text{ km}$ and the Sverdrup transport is approximately 40 Sv , the westward velocity near the western boundary is approximately $40 \times 10^6 \text{m}^3 \text{s}^{-1} / (1000\text{m} \times 1250\text{km}) \simeq 0.036 \text{m s}^{-1}$. This yields an inertial boundary layer with a width of $\sqrt{3.6 \times 10^{-2} / \beta} \simeq 40\text{ km}$. Therefore, δ_I is approximately 0.9. Although the width of the viscous boundary layer in the real ocean is unknown, it would be less than the inertial boundary layer width. In the numerical experiment of Nakano et al. (2008), δ_M was approximately 0.4; but they used bi-harmonic viscosity. In the present study, $\delta_M = 0.3$ was used as the reference value that corresponded to $\nu = 50 [\text{m}^2 \text{s}^{-1}]$. Ierley and Ruehr (1986) showed that for steady broad eastward flow from a nonlinear Munk layer to exist, a parameter $\lambda = \left(\frac{\delta_I}{\delta_M}\right)^2 \hat{U}$ is smaller than about 0.8, where \hat{U} is the eastward velocity in the interior. Since $(\delta_I/\delta_M)^2$ in typical case in this study was nearly 10, it was expected that the condition could not be satisfied almost anywhere; hence, the eastward flow is expected to be a narrow jet accompanying recirculation gyres (Ierley, 1987).

Although most experiments are conducted with single-gyre forcing ($Y_S = -1$ and $Y_N = 0$), which produced a subtropical circulation, it is assumed that an anti-symmetric subarctic circulation on the outside of the northern boundary using the slip boundary condition. Therefore, mass conservation was satisfied automatically. The next section describes the differences among experiments in double-gyre ($Y_S = -1$ and $Y_N = 1$) as well as in single-gyre conditions. From the initial state with no flow in the upper and lower layers, time integration was conducted over a range greater than 100,000 non-dimensional times (80 years) which is 25 times longer than the baroclinic Rossby wave response time. A quasi-equilibrium state was established after approximately 20,000 non-dimensional times.

2.2 IDO-CF scheme

In the present study, the IDO-CF (conservative form of the interpolated differential operator) scheme developed by Imai et al. (2008) is used. In particular, the IDO-CF scheme has the advantage of calculating the advection term. Even if one value in the field changes abruptly in a short space, the IDO-CF scheme can calculate these changes without numerical oscillations, thus retaining the conservative quantity. In the western boundary current extension jet region, the extension jet is the boundary where the areas with significantly different potential vorticity values are contiguous. Figure 2 shows a result of solving the advection equation using IDO-CF scheme without viscosity term, for example. In spite of giving the abrupt change of q between one grid, the distribution changes much little.

Figure 3 shows the collocation of defined points in this scheme, where

$$\begin{aligned}
 {}^x q_{i+1/2,j} &= \int_{x_{i,j}}^{x_{i+1,j}} q dx, \quad {}^y q_{i,j+1/2} = \int_{y_{i,j}}^{y_{i,j+1}} q dy \quad \text{and} \\
 {}^{xy} q_{i+1/2,j+1/2} &= \int_{x_{i,j}}^{x_{i+1,j}} \int_{y_{i,j}}^{y_{i,j+1}} q dy dx
 \end{aligned}$$

as a line integral of 1 grid width at the cell interface in the x-direction, in the y-direction and a double integral in the x-direction and y-direction, respectively. Temporal evolution of these quantities are calculated by the 4th order Runge Kutta scheme, as well as $q_{i,j}$, and they provide high accurate spatial differentiations. For examples, the first order partial differential is

$$\frac{\partial q}{\partial x_{i,j}} = \frac{2}{\Delta x^2} ({}^x q_{i+\frac{1}{2},j} - {}^x q_{i-\frac{1}{2},j}) - \frac{1}{2\Delta x} (q_{i+1,j} - q_{i-1,j})$$

and second order partial differential is

$$\frac{\partial^2 q}{\partial x_{i,j}^2} = \frac{15}{2\Delta x^3} ({}^x q_{i+\frac{1}{2}} + {}^x q_{i-\frac{1}{2}}) - \frac{3}{2\Delta x^2} (q_{i+1} + 8q_{i,j} + q_{i-1})$$

In the numerical experiments, the grid size, Δx and Δy for the x-direction and y-direction, respectively, were set to 1/256 to coincide with the minimum viscous boundary layer width. Because the cell-integrated values are also calculated, the assumed grid size is regarded as the half size of Δx and Δy . For several cases, numerical experiments were conducted using the half grid size ($\Delta x = \Delta y = 1/516$) to confirm that there is no significant difference.

Chapter 3

Results

3.1 Two typical solutions

Although the discussions of the dynamics of the separation of western boundary current and forming eastward jet mainly based on the results of single-gyre experiments, the author describes typical solutions that appear in double-gyre experiments because double-gyre experiments are much more commonly used for studying basic ocean dynamics, as attempted in this study. Figures 4 and 5 show the streamfunctions and potential vorticity for $\hat{w}_e = \sin \pi y$ with the meridional extent of $-1 < y < 1$ for two typical solutions. One solution is characterized by double eastward jets that separate prematurely from the western boundary (Fig. 4), and the other is characterized by a single eastward jet along the subtropical/subpolar gyre boundary (Fig. 5). Although these solutions are very different with each other, the parameter values differ only for δ_M ($\delta_M = 0.3$ in the former case and 0.22 in the latter case); the other parameters are common ($\delta_I = 0.9$, $H_1/H_2 = 1/4$, $\hat{r} = 10^{-3}$, $\alpha = 5.7 \times 10^2$). We refer to the former solution as the ‘prematurely separated jet case’ and the latter as the ‘gyre boundary jet case’.

In the prematurely separated jet case, the western boundary current separate from the boundary, and the strong eastward extended jet is formed at latitude of approximately

-0.2 in the southern half (subtropical) region, accompanied by northern and southern recirculation gyres on both sides. Although there are many eddies in the snapshots (upper panels in Fig. 6), we can clearly find two meandering narrow jets. Thus, the structure of the temporal mean jets can be substantial. In Fig. 4, the jet is located along the front of low (high) potential vorticity water advected by the inertial boundary current and high (low) potential vorticity water generated by the viscous boundary layer in the subtropical (subpolar) region as in Kiss (2002). Northern and southern recirculation gyres in the flank of the jet, mentioned in Nakano et al. (2008), is also seen in both the upper and lower layers, which imply that these recirculations create strong barotropic structure. The velocity of the jet is rapidly damped for $x > 1.0$, where the ocean is forced by the Ekman pumping velocity, and it is smoothly connected to the interior Sverdrup flow region. The jet length of the time mean field, defined as the distance from the western boundary to the western most position, where the maximum velocity falls below the half of the averaged velocity of the jet from $x = 0.5$ to $x = 1.0$, is approximately 1.1. Note that the eastern edge of the jet exhibits such large fluctuations that the zonal jet seen in snapshots extends longer than that in the time mean field. Time mean streamfunction field is almost anti-symmetric at the gyre boundary. Figure 7 shows the meridional profiles of potential vorticity (left), $Q_j(y)$, and the streamfunction (right), $\Psi_j(y)$; both averaged from $x = 0.5$ to $x = 1.0$ for the time mean. The potential vorticity tends to be homogenized at the northern and southern sides of the jet in the upper layer and below the jet in the lower layer. In the southern half region, $\Psi_1(y)$ and $Q_1(y)$ are consistent with the values estimated by Sverdrup balance:

$$\hat{\psi}_{Sv}(y) = -\hat{w}_e(y) \quad \text{and} \quad \hat{q}_{Sv}(y) = \frac{1}{\hat{\beta}} \left(\frac{\partial^2 \hat{\psi}_{Sv}}{\partial y^2} - F_I \frac{H_2}{H_0} \hat{\psi}_{Sv} \right) + y, \quad (3.1)$$

where $\hat{\psi}_{Sv}(y)$ and $\hat{q}_{Sv}(y)$ are ψ_{Sv} and q_{Sv} in the western part of the basin.

In the gyre boundary jet case, the single jet is located at the gyre boundary, and there is extensive anticyclonic and cyclonic recirculation on its southern and northern

sides, respectively (Fig. 5). The jet length is approximately 1.3, which is much further than that in the prematurely separated jet case, and the mean velocity of the jet is about three times higher than that in the prematurely separated jet case. The potential vorticity tends to be homogenized on the both sides of the jet and the Ψ_1 consistet with ψ_{Sv} in the region far from the jet as the same as that for the prematurly separated jet case (Fig. 7).

Next, we compare the results obtained using single-gyre forcing with double-gyre forcing (Figs. 4, 5 and 7). In the prematurely separated jet case, there is little difference between a single-gyre case(Fig. 8) and a double-gyre case(Fig. 4) in the subtropical region; the meridional profiles of the streamfunction and the potential vorticity are also almost the same (upper panels in Figs. 7 and 9).

In the gyre boundary jet case with single-gyre forcing, the jet is located at the northern boundary, and there is an extensive and robust anticyclonic recirculation on its southern side (Fig. 10). The jet reaches the eastern boundary. The elongation of the northern boundary jet is considered to be caused by a hypothetical vortex pair that stably progresses to the eastern boundary by self-advection, presumably because of the anti-symmetric solution given by the slip boundary condition on the northern boundary. Under the conditions of double-gyre forcing, shear instability occurs on the gyre boundary jet, and the elongation of the jet is reduced. As a result, the strength of the circulation with single-gyre forcing is quite large compared to the double-gyre case because there is no lateral vorticity mixing through the northern boundary, which was mentioned by Fox-Kemper (2005) in a barotropic model.

Although there are many differences between single and double gyre forcing in the gyre boundary jet case, the prematurely separated jet case is more important, because it seems to correspond to realistic eastward jets, where single and double gyre forcing yield almost the same results; the classification of the solution type for the parameters does not change either. We are interested in the dependence of the jet separation latitude

on parameters. Therefore, the parameter dependence of the solution using single gyre forcing with $Y_S = -1$ and $Y_N = 0$ is examined to save computing resources in the following subsections.

3.2 Dependence on parameters

3.2.1 Dependencies on viscous and inertial boundary layer width

The dependence of the latitude of the eastward extended jet on δ_I and δ_M in the temporal mean field is investigated. The latitude of the jet, Y_{Jet} , is defined as the y value at which took the maximum time mean zonal velocity zonally averaged from $x = 0.5$ to $x = 1$ occurred.

The parameter ranged from 0.2 to 0.3 for δ_M and from 0.82 to 1.06 for δ_I . The experiment was also conducted under $\delta_M = 0.4$, which was hardly different from the case in which $\delta_M = 0.3$. Because dimensional velocity in the model is proportional to δ_I^2 , the set range of δ_I corresponds to 0.8 to 1.4 times the strength of the flow of the typical case in which $\delta_I = 0.9$.

Figure 12(a) shows the latitude of the jet in the $\delta_M - \delta_I$ plane. When δ_I is larger and δ_M is smaller, the gyre boundary jet case tends to occur. In the case of premature separation, the temporal variation of Y_{Jet} is approximately 0.03, which is larger than the difference in Y_{Jet} caused by changes in the parameters. Therefore, Y_{Jet} is regarded as approximately -0.2 in these cases, independent of the parameters. We found that the flow pattern tends to be the premature separated jet case for large δ_M^3/δ_I^2 to which the Reynolds number was proportional and to be the boundary jet case for small δ_M^3/δ_I^2 , as expected from Fig. 12(a). However, the two cases coexist in the medium range of δ_M^3/δ_I^2 , which suggests the solution type is not determined only by δ_M^3/δ_I^2 . Figure 12(b) shows the jet length in the $\delta_M - \delta_I$ plane. It also has little dependence on parameters for

the prematurely separated jet case, although its length tends to increase with increasing δ_I . In the gyre boundary jet case, temporal variation in Y_{Jet} does not occur except for the initial transient; the value remains at $Y_{Jet} = 0.0$, and the jet extends to the eastern boundary in all cases.

Experiments with other initial conditions were also conducted. In the parameter range that showed a gyre boundary jet, similar experiments were conducted with the initial conditions set as the time mean solution of a premature separation case calculated using slightly different parameters. Except for the cases in which $\delta_M = 0.2$ and $\delta_I = 1.06$, the quasi-steady solutions showed prematurely separated jets. The observed dependence on the initial conditions indicates the existence of multiple equilibrium solutions. With the initial conditions set to the solution of the gyre boundary jet case, Y_{Jet} was 0.0 over the entire parameter range of Fig. 12. Once an extension jet is formed along the free-slip northern boundary, the structure of boundary jet is quite robust and hardly collapses. For much smaller δ_I of 0.58 and $\delta_M = 0.3$ (not shown), even if the initial condition was the gyre boundary separation type, the solution eventually evolved to a prematurely separated jet. However in such a case, because the jet separated from the western boundary declines immediately and did not extend enough, the author did not address such weak jet cases in detail below.

It is important that Y_{Jet} is constant at approximately -0.2 for various δ_M and δ_I in the prematurely separated jet case. This case has no intermediate solution with $Y_{Jet} = -0.10$, for example.

3.2.2 Dependence on boundary condition

In the experiment conducted by Haidvogel et al. (1992), premature separation did not occur under free slip western boundary conditions; however, when the partial-slip coefficient, α , increased, and the boundary condition approached the no-slip condition,

premature separation was observed. This suggests that the generation of positive vorticity in the viscous boundary layer is important for premature separation to occur (Kiss, 2002). As seen in Fig. 8, when the premature separation occurs, high potential vorticity fluid is accumulated in the northern recirculation gyre. This high potential vorticity is generated on the western side of the boundary current, while the low potential vorticity in the southern recirculation gyre is advected from the south. Since the western boundary current is a narrow jet, total relative vorticity integrated over the boundary layer almost vanishes, when the no-slip boundary condition is applied. This could be related to a symmetric structure of northern and southern recirculation gyres. Since the zero total relative vorticity always holds independent of δ_I and δ_M , it could explain the independence of the latitude of prematurely separated jet from the parameters. So, a series of experiments with the partial slip boundary condition which would tend to give negative total relative vorticity were conducted and the dependence of latitude of the extension jet on the partial slip coefficient α was investigated. In this series of experiments, $\delta_M = 0.3$ and $\delta_I = 0.9$; the values of the other parameters were the same as those in the previous experiments. The dependence of Y_{Jet} on the partial-slip coefficient is shown in Fig. 13 (a). As the partial-slip coefficient decreased, the regime changed from the prematurely separated jet case to the gyre boundary jet case. These characteristics are qualitatively consistent with that in Haidvogel et al. (1992), although the value of α where the regime transition occurs is larger than that in Haidvogel et al. (1992) (while the value is from 3 to 6.5 in their experiment, it is estimated to be about 48 to 61 for in the present study using their scaling). However, the regime also depends on the initial conditions, so a single critical value of α cannot be defined. Haidvogel et al. (1992) also saw a gradual transition but present result of it was abrupt. In the experiments of Haidvogel et al. (1992), broad oscillation of the western boundary current separation point was observed at relatively small α ; however, such broad oscillation did not occur in present experiments. These discrepancies would come from the differences in the viscosity term for which they used

the bi-harmonic form, and/or existence of a slip northern boundary. The value of Y_{Jet} is nearly -0.2 independent of α and total positive vorticity (see also Fig. 13 (b)) when the premature separation occurs. This result supports the idea that Y_{Jet} does not depend on detailed structure of the western boundary region in a prematurely separated jet case.

3.2.3 Other parameters

As mentioned in Chapter 2, the ratio of the thickness of the upper and lower layers (H_1/H_2) was also a parameter that determined the circulation pattern in this model. The ratio of H_1 to H_2 is closely related to baroclinic instability. When the upper layer eastward velocity is U_1 and the lower layer is at rest, the necessary condition of baroclinic instability is $U_1 > \hat{\beta}/F_2 = 2(1 + H_2/H_1)\delta_I^{-2}$. As H_1/H_2 increases, the instability becomes stronger. Because the baroclinic instability tends to mix the potential vorticity in the lower layer, the meridional width of the potential vorticity homogenized region in the lower layer tends to be narrower and barotropic recirculation gyres are weakened as H_1/H_2 decreases.

Figure 14 shows the results of experiments performed under four different values of H_1/H_2 with the no-slip western boundary condition and $(\delta_M, \delta_I) = (0.3, 0.9)$, i.e., the same values used in the previous section. Here, the value of H_1/H_2 changed from 1/1 to 1/16. If the other dimensional parameters including R_d are fixed as in Table 1, H_1 and H_2 used for the experiments in Fig. 14 correspond to $(H_1, H_2) \approx (1600[\text{m}], 1600[\text{m}])$, $(1200[\text{m}], 2400[\text{m}])$, $(900[\text{m}], 7200[\text{m}])$ and $(850[\text{m}], 13600[\text{m}])$ respectively. Smaller H_1/H_2 was associated with weaker flow in the lower layer. In the case with $H_1/H_2 = 1/8$, there was still a closed contour under the southern recirculation; the pattern of the ψ_2 contours is similar to the case with $H_1/H_2 = 1/4$ (Fig.8d). When $H_1/H_2 = 1/16$ the western boundary current did not separate until it reached the northern boundary. In this case, the lower layer was almost at rest. This suggests that an

active lower layer is important for premature separation to occur in rectangular basin, although the reason is still not clear. This is consistent with the experiments by Pierini (2006), who used a 1.5-layer model, in which the latitude of the extension jet seems realistic; however, relative to the Sverdrup circulation, the jet was located along the gyre boundary. To confirm the necessity of two active layers, experiments using a one-layer barotropic model and a 1.5-layer model were carried out. The quasi-steady solutions of these models showed the gyre boundary jet case, even when the streamfunction in the prematurely separated jet case was given as their initial conditions (not shown).

In the cases of $H_1/H_2 = 1/2$ and $1/8$, premature separation occurred as in the standard case. In these cases, Y_{Jet} was also nearly -0.2 . This suggests that Y_{Jet} is also almost independent of H_1/H_2 once premature separation occurs. For $H_1/H_2 = 1$, the flow pattern was of the gyre boundary jet type. However the anti-cyclonic recirculation gyre near the northern boundary occupied more than one fourth of the entire basin and formed a much stronger circulation than in the previous experiments. The vigorous horizontal mixing caused by the baroclinic instability produced a wide region of homogenized potential vorticity in the lower layer, and this homogenized region generated the barotropic anti-cyclonic gyre along the boundary. In the double-gyre case, while the gyre boundary jet occurred, strong circulation of this type was not formed because of the potential vorticity mixing through the subpolar/subtropical inter-gyre boundary.

In addition to the basic value of $\hat{r} = 10^{-3}$, dependence of Y_{Jet} on \hat{r} was also investigated for the values of 0 and 10^{-4} under $\delta_M = 0.3$, $\delta_I = 0.9$ and $H_1/H_2 = 1/4$. All values of \hat{r} produced premature separation and Y_{Jet} was also -0.2 , although many more eddies were observed for smaller \hat{r} (Fig. 15).

3.2.4 The Influence due to Symmetry

In all above experiments, symmetric structure has been assumed to northern boundary or symmetric forcing has been used for double gyre circulations. Two different types of solutions were found and the initial conditions could depend on the solution type. It indicated the existence of multiple equilibrium solutions. In symmetric double gyre cases, the initial gyre boundary jet is maintained at gyre boundary. Figure 16 shows the result when the Ekman pumping velocity for $y > 0$ was set to zero as a non-symmetric distribution to $y = 0$. The prematurely separated jet was formed and Y_{Jet} was nearly -0.2 even if the initial condition was gyre boundary jet. Figure 17 shows the result when Y_N was set to 1 and the Ekman pumping velocity for $y > 0$ was set to zero with slip boundary condition. Branched western boundary current reaches the northern boundary and forms anti-cyclonic recirculation gyre where the negative vorticity can be diffused. After that, the fluid returns to the extension jet region and forms cyclonic recirculation gyres. Even if the western boundary condition was slip, premature separation occurred under the non-symmetric forcing. Above two suggests that the presence of meridional symmetry in the gyre boundary makes the structure of the gyre boundary jet robust and gives rise to multiple solutions.

3.3 Dependence on Meridional Distribution of Ekman Pumping Velocity

As shown in the previous subsections, the latitude of the eastward jet hardly depends on $\delta_M, \delta_I, H_1/H_2, \hat{r}$ and α once premature separation occurs. In addition, Nakano et al. (2008) showed that the latitude of the extension jet does not depend on the shape of the western boundary. These results lead us to expect that the factor that determines the latitude of the extension jet is the distribution of external forcing.

3.3.1 Setting on Distributions of the Ekman Pumping Velocity

In all previous experiments, the meridional distribution of the Ekman pumping velocity, \hat{w}_e was $\sin \pi y$. In this subsection the dependence of the latitude of the extension jet on the distribution of \hat{w}_e is investigated with $(\delta_M, \delta_I) = (0.3, 0.9)$, $H_1/H_2 = 1/4$, $\hat{r} = 10^{-3}$ and the no-slip western boundary condition. The distributions of Ekman pumping velocity investigated here are summarized in Fig. 18 and Table 3; S_k are sinusoidal, L_k are triangular ($k=1$ to 3), and X_1 is of cusp shape. In the L_2 case, δ_I was set to 1.1, because the strength of the jet was weakened by widening the eastward Sverdrup flow region in the meridional direction, and the jet length was short relative to the other cases under the same value of δ_I .

3.3.2 Results

Fig. 19 shows the meridional distribution of the zonal mean potential vorticity and streamfunction for L_1 , X_1 , and L_2 . The values of $Q_1(y)$ and $\Psi_1(y)$ are consistent with the values estimated by the Sverdrup balance except for near the jet region similar to S_1 case (see Fig. 9b), although they are slightly different near the center of the gyre where $\frac{\partial \hat{\psi}_{Sv}}{\partial y}$ is discontinuous but ψ_1 is smooth. In contrast to the results of previous subsections, the latitude of the jet is significantly different for each \hat{w}_e , as shown in Fig. 20 (a) and Table 3. The figure indicates two trends in Y_{Jet} . The first is that Y_{Jet} tends to shift in the direction in which the center of the Sverdrup circulation corresponding to the latitude of maximum $|\hat{w}_e|$, Y_C , is shifted. The second, Y_{Jet} depends on the curvature of the meridional distribution of \hat{w}_e ; a larger curvature is associated with smaller $|Y_{Jet}|$, which could be confirmed by comparing the S_1 , L_1 , and X_1 cases. Because of Eq. (3.1), with the same Y_C , Y_{Jet} in the case with positive (negative) curvature of $\hat{\psi}_{Sv}$, $\frac{d^2 \hat{\psi}_{Sv}}{dy^2}$, occurs at a higher (lower) latitude than in the case with zero curvature of $\hat{\psi}_{Sv}$.

Because the extension jet connects to the Sverdrup interior region smoothly and the

contours of all streamfunction values concentrate in the jet region, it is expected that the streamfunction of the center of the jet, $\Psi_{Jet}(= \Psi_1(Y_{Jet}))$, would be close to the average of the minimum and maximum $\hat{\psi}_{Sv}$ values, which was 0.5 in the experiments in present study. Figure 20(b) shows the relation between Y_{Jet} and the y -coordinate where $\hat{\psi}_{Sv} = 0.5$ (hereafter $Y_{Sv}(0.5)$). The correlation between Y_{Jet} and $Y_{Sv}(0.5)$ is better than that between Y_{Jet} and Y_C . When the curvature of $\hat{\psi}_{Sv}$ is negative (i.e., $\frac{d^2\hat{\psi}_{Sv}}{dy^2} < 0$) as S_1 case, $Y_{Sv}(0.5)$ shifts northward, and vice versa, although Ψ_{Jet} varies between 0.4 and 0.6 (see Fig. 21a). The difference of Ψ_{Jet} from 0.5 probably comes from asymmetry of the jet and reduction of the $\Psi_1(Y_C)$ value for a smooth connection in the case with discontinuous $\left. \frac{\partial\hat{\psi}_{Sv}}{\partial y} \right|_{y=Y_C}$ as seen in Fig. 19.

3.3.3 Integral Condition for Streamfunction in the Western Region

The above discussion roughly interprets the dependency of Y_{Jet} on the meridional profile of \hat{w}_e , which suggests that Y_{Jet} would be equal to the y -coordinate where $\hat{\psi}_{Sv}(y) = \Psi_{Jet}$, $Y_{Sv}(\Psi_{Jet})$. However, Figure 21(b) shows that the difference between Y_{Jet} and $Y_{Sv}(\Psi_{Jet})$ is large in S_1 and S_3 cases, as compared with that in cases S_2 , L_k and X_1 . As the curvature in S_2 is negative but its magnitude is much smaller than that in S_1 around $y = Y_{Jet}$, Fig. 21(b) suggests that negative curvature in $\hat{\psi}_{Sv}$ tends to shift the jet southward.

To illustrate this, an integral condition given in the western part of the basin was considered. It is derived from the potential vorticity equations, Eq. (2.3) in the upper layer, integrated from Y_S to Y_N in the meridional direction and from X_E to an arbitrary longitude in the western half region, x , in the zonal direction outside the western boundary current region. The area integration of Eq. (2.3) yields

$$\int_{Y_S}^{Y_N} \int_{X_E}^x \left[\frac{\partial q_1}{\partial t} + \frac{1}{\beta} \left\{ \frac{\partial}{\partial x} \left(-\frac{\partial \psi_1}{\partial y} q_1 \right) + \frac{\partial}{\partial y} \left(\frac{\partial \psi_1}{\partial x} q_1 \right) \right\} \right] dx dy = \int_{Y_S}^{Y_N} \int_{X_E}^x w_e dx dy, \quad (3.2)$$

where it is assumed that the viscous terms are sufficiently small and are neglected. With boundary conditions of no normal flow, (3.2) reduces to

$$\frac{\partial}{\partial t} \int_{Y_S}^{Y_N} \int_{X_E}^x q_1 dx dy - \frac{1}{\hat{\beta}} \int_{Y_S}^{Y_N} \left. \frac{\partial \psi_1}{\partial y} q_1 \right|_x dy = \int_{Y_S}^{Y_N} \int_{X_E}^x w_e dx dy . \quad (3.3)$$

Using Eq. (2.4), $\psi_1|_{y=Y_S} = \psi_1|_{y=Y_N} = 0$ and the Sverdrup balance ($\frac{\partial \psi_{Sv}}{\partial x} = w_e$) and averaging in time, we obtained

$$\begin{aligned} -\frac{1}{\hat{\beta}} \left[\frac{1}{2} \left(\frac{\partial \bar{\psi}_1}{\partial y} \right)^2 \right]_{Y_S}^{Y_N} + \frac{1}{\hat{\beta}} \int_{Y_S}^{Y_N} F_I \frac{H_2}{H_0} \frac{\partial \bar{\psi}_1}{\partial y} (\bar{\psi}_1 - \bar{\psi}_2) \Big|_x dy - \frac{1}{\hat{\beta}} \int_{Y_S}^{Y_N} \left. \frac{\partial \bar{\psi}'_1}{\partial y} q'_1 \right|_x dy \\ + \int_{Y_S}^{Y_N} \bar{\psi}_1 \Big|_x dy = \int_{Y_S}^{Y_N} \hat{\psi}_{Sv} dy \end{aligned} \quad (3.4)$$

where over-bars represent the time mean, q'_1 and ψ'_1 are defined as $q_1 - \bar{q}_1$ and $\psi_1 - \bar{\psi}_1$, respectively, and $\frac{\partial^2}{\partial x^2} \ll \frac{\partial^2}{\partial y^2}$ for $\bar{\psi}_1$ is assumed. If the mass transport through the longitude in question is zero, the second terms can be ignored ($O(10^{-2})$ compared to the fourth term on the left hand side actually). In the prematurely separated jet case, because $\bar{\psi}_1 \approx \hat{\psi}_{Sv}$ far from the jet, or $\frac{\partial \bar{\psi}_1}{\partial y}$ is of the same order as $\frac{d\hat{\psi}_{Sv}}{dy}$ at the boundary, the first term on the left hand side is sufficiently small $O(10^{-3})$ and can be ignored. The third term is left but the order was $O(10^{-2})$ in all experiments of this study with a prematurely separated jet. Therefore the three terms multiplied by $\frac{1}{\hat{\beta}}$ are ignored and

$$\int_{Y_S}^{Y_N} \bar{\psi}_1 dy \approx \int_{Y_S}^{Y_N} \hat{\psi}_{Sv} dy \quad (3.5)$$

is obtained.

Figure 22 is the plot of the meridional integral of $\hat{\psi}_{Sv}$ and that of the time and spatial averaged ψ_1 and shows that Eq. (3.5) is substantially satisfied in all cases.

Figure 23 is the schematic to interpret the relation of Y_{Jet} and Eq. (3.5) above. Equation (3.5) states that the area A is equal to the area B in Fig. 23. When $\frac{d^2 \hat{\psi}_{Sv}}{dy^2} = 0$, Y_{Jet} coincides with $Y_{Sv}(\Psi_{Jet})$ as in the left panel. On the other hand, when $\frac{d^2 \hat{\psi}_{Sv}}{dy^2} < 0$

as in $\hat{w}_e = \sin \pi y$, Y_{Jet} must be smaller than $Y_{Sv}(\Psi_{Jet})$ if Ψ_{Jet} is the mean of the local maximum and minimum of $\Psi_1(y)$ on either side of the jet. (It was confirmed that the mid point between the local maximum and minimum of Ψ_1 coincided with Y_{Jet} within the width of one grid cell in experimental results). This explains the relation between Y_{Jet} and $Y_{Sv}(\Psi_{Jet})$ for S_1 and S_3 cases. Similarly, this explanation makes us to expect that $Y_{Jet} = Y_{Sv}(\Psi_{Jet})$ for L_k cases and $Y_{Jet} > Y_{Sv}(\Psi_{Jet})$ for X_1 case, but Y_{Jet} was slightly smaller than $Y_{Sv}(\Psi_{Jet})$ for L_k cases and Y_{Jet} was almost equal to $Y_{Sv}(\Psi_{Jet})$ for X_1 case. This discrepancy perhaps comes from the distortion of the upper layer streamfunction field caused by the discontinuity in $\frac{\partial \psi_{Sv}}{\partial y}$ at $y = Y_C$ as seen in Fig. 19.

Therefore, The Ψ_{Jet} value tends to take a value around the mean between the maximum and minimum of $\hat{\psi}_{Sv}$, and the jet axis, Y_{Jet} , is located slightly to the south of the latitude expected from $\hat{\psi}_{Sv}(y) = \Psi_{Jet}$ for the case of $\hat{w}_e = \sin \pi y$.

Chapter 4

Conclusions and Remarks

The parameter dependence of the latitude of the eastward extension jet that separates from the western boundary was investigated using a two-layer quasi-geostrophic model in a rectangular basin. The investigated parameters included the inertial boundary layer width, δ_I , the viscous boundary layer width, δ_M , the partial-slip coefficient, α , the ratio of the upper layer and lower layer thickness, H_1/H_2 , and the coefficient of bottom friction, \hat{r} . It was shown that the patterns of circulation that included the extension jet could be classified into two patterns. One is the ‘prematurely separated jet case’, and the other is the ‘gyre boundary jet case’. When δ_I is smaller and δ_M is larger than certain values, the solution tended to show the premature separation pattern where the change occurs abruptly, and there is no intermediate solution. Meanwhile, in the parameter range investigated, almost everywhere there are multiple solutions depending on initial conditions. Such character is common in many previous studies on the nonlinear ocean circulation (e.g. Jiang et al., 1995; Cessi and Ierley, 1995; McCalpin and Haidvogel, 1996; Primeau and Newman, 2007). Present result is different from the result obtained using a 1.5-layer model driven by double-gyre wind forcing (Jiang et al., 1995) which showed continuous change of separation latitude with strength of the forcing as well as from the result obtained using a barotropic model (Cessi and Ierley, 1995). Their

variation of the separation point is caused by an asymmetric structure with a confluent point of southward and northward western boundary currents. In 1.5-layer model and barotropic model experiments, the prematurely separated jet is not seen even when the initial condition is of the prematurely separated jet case.

For the prematurely separated jet case, $\delta_M, \delta_I, H_1/H_2$ and \hat{r} have little impact on Y_{Jet} . In addition, Y_{Jet} does not depend on the western boundary condition in this case. These findings suggest that when premature separation occurs Y_{Jet} is independent of the detailed configuration of the western boundary. In contrast, it was found that Y_{Jet} was strongly affected by the meridional distribution of the Ekman pumping velocity, w_e .

The author especially studied the effects on Y_{Jet} of the location at the center of the Sverdrup circulation and the curvature of the Sverdrup streamfunction in the western basin ($\hat{\psi}_{Sv}$). It was found that the streamfunction value at the jet, Ψ_{Jet} , tends to take a value around half of the streamfunction at the center of the Sverdrup circulation, and the jet axis, Y_{Jet} , is located slightly to the south of the latitude expected from $\hat{\psi}_{Sv}(y) = \Psi_{Jet}$ for the case of $\hat{w}_e = \sin \pi y$. In the real ocean, the central latitude of the Sverdrup circulation for the subtropical region is approximately 30°N, the gyre boundary of the subtropical and subpolar gyre is approximately 46°N as estimated by zonal mean wind stress curl (Milliff et al., 2004), the latitude of the Kuroshio extension is approximately 34°N, and the median latitude of the maximum Sverdrup streamfunction is about 35°N (Nakano et al., 2008). Present results are qualitatively consistent.

Meanwhile the integral condition of Eq. (3.5) is satisfied in all experiments. From (3.5), the relationship for potential vorticity is directly derived as

$$\int_{Y_S}^{Y_N} \bar{q}_1 dy \approx \int_{Y_S}^{Y_N} \hat{q}_{Sv} dy, \quad (4.1)$$

which means that \hat{q}_{Sv} was redistributed to the meridional distribution of the potential vorticity, q_1 , in the region involving the extension jet or recirculations. This supports the above conclusion that Y_{Jet} is more influenced by the interior Sverdrup region than by the

western boundary layer region.

In the present study, a forcing in the western half of the region was not provided. However, because wind above a real ocean blows across the entire basin, the extension jet would be affected by wind forcing, which caused the reduction of the jet length (see Fig.8 and Fig.16). Because the jet connects to the Sverdrup region at the tip of the jet, it is necessary to understand the effect of the southward Sverdrup flow on the jet length and jet latitude more accurately.

Acknowledgment

I am deeply grateful to Prof. Atsushi Kubokawa who provided carefully considered feedback, valuable comments. Special thanks also go to Prof. Humio Mitsudera , Dr. Takeshi Horinouchi, Dr. Genta Mizuta, and Dr. Hideyuki Nakano who provided sincere encouragement. GFD-DENNOU Library was used for drawing figures. Numerical calculations were partly performed on the HITAC SR16000, Hokkaido University.

Figures

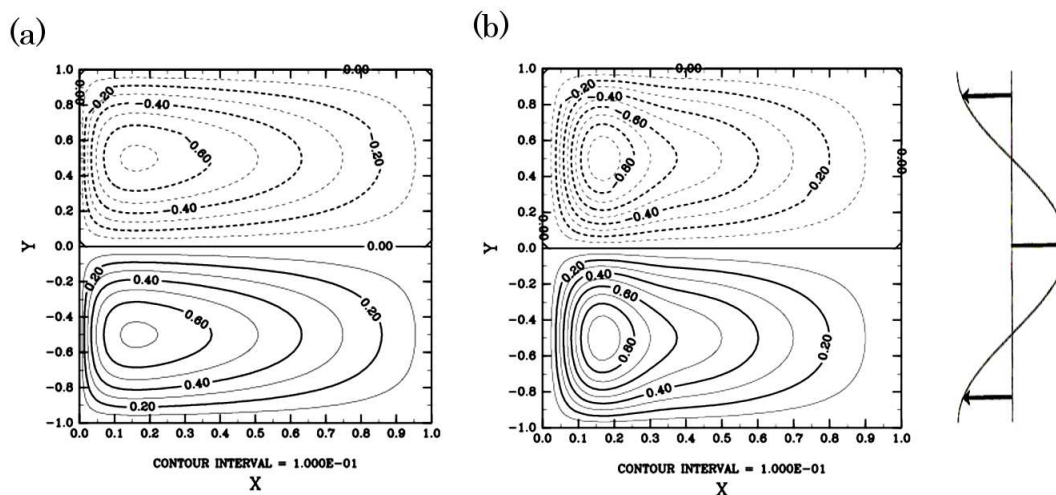


Figure 1: Linear solutions. (a) The streamfunction of Stommel model; (b) That of Munk model with Ekman pumping velocity to $\sin \pi y$. The domain length is 2.

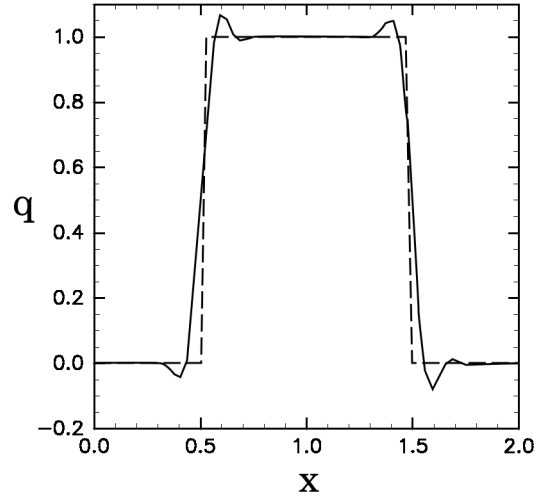


Figure 2: Numerical solution of advection equation of rectangular wave. The solid line indicates using IDO-CF scheme; the dashed line indicates initial.

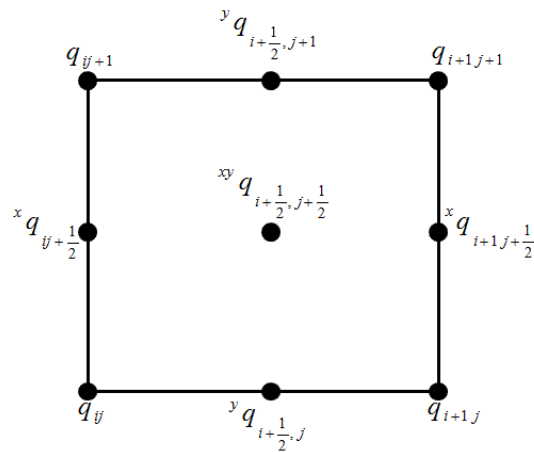


Figure 3: Configuration of variables on grids for the IDO-CF scheme.

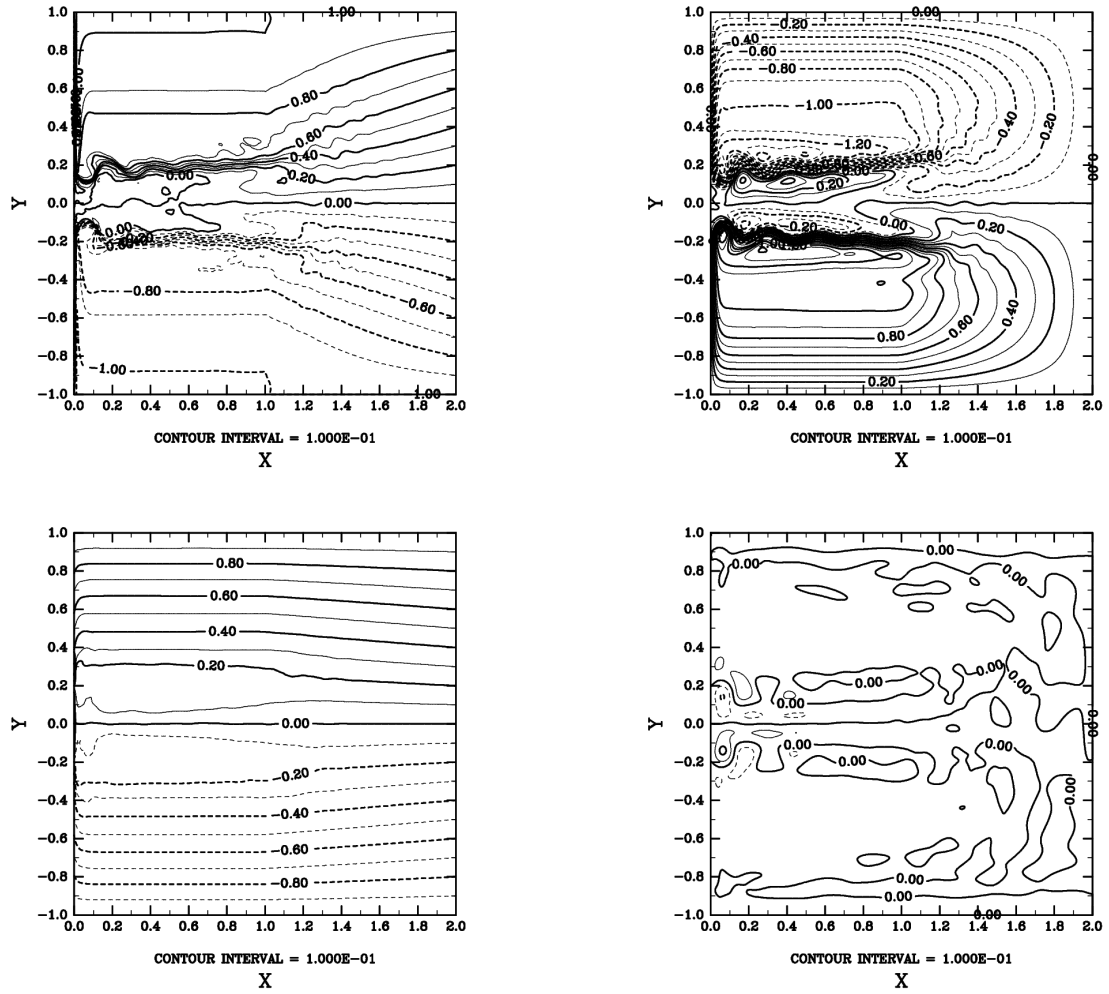


Figure 4: The temporal mean potential vorticity (left) and streamfunction (right) fields driven by a double-gyre forcing in the prematurely separated jet case ($\delta_M = 0.3, \delta_I = 0.9$). The upper and lower panels show the upper and lower layers, respectively.

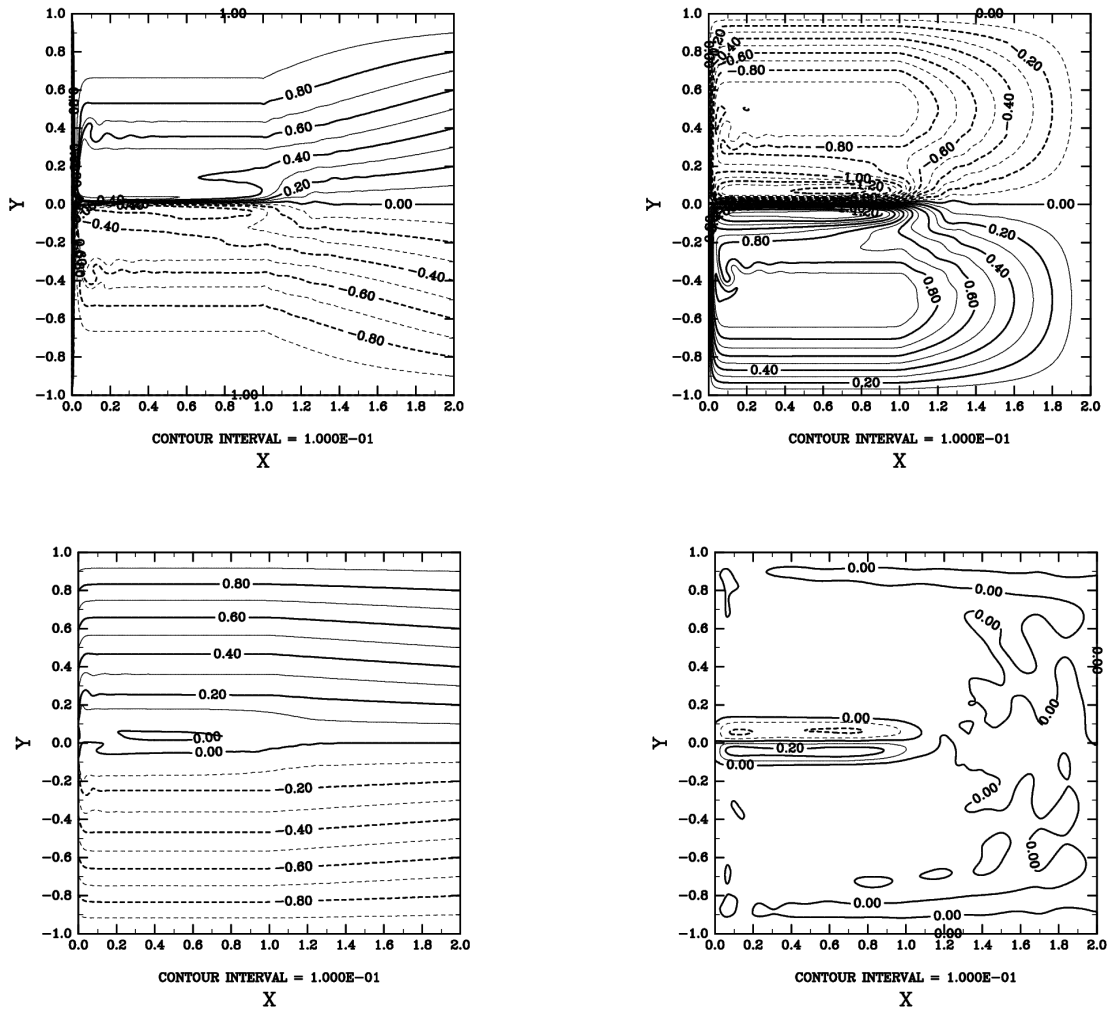


Figure 5: Same as Fig. 4 but for the gyre boundary jet case ($\delta_M = 0.22, \delta_I = 0.9$)

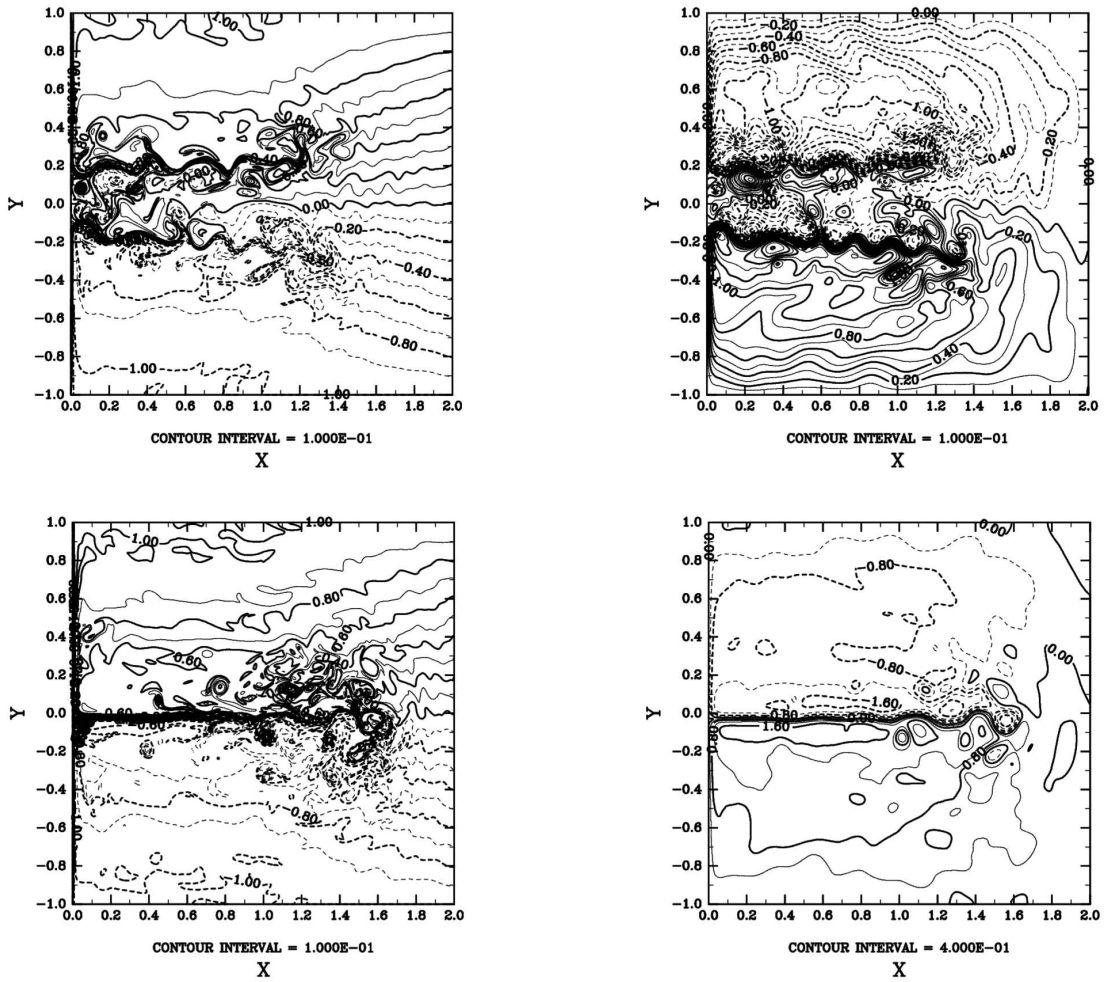


Figure 6: Snapshots of two typical solutions in the upper layer ($t=100,000$). (Left) potential vorticity; (right) streamfunction. (Upper) $\delta_M = 0.3$, $\delta_I = 0.9$; (lower) $\delta_M = 0.22$, $\delta_I = 0.9$.

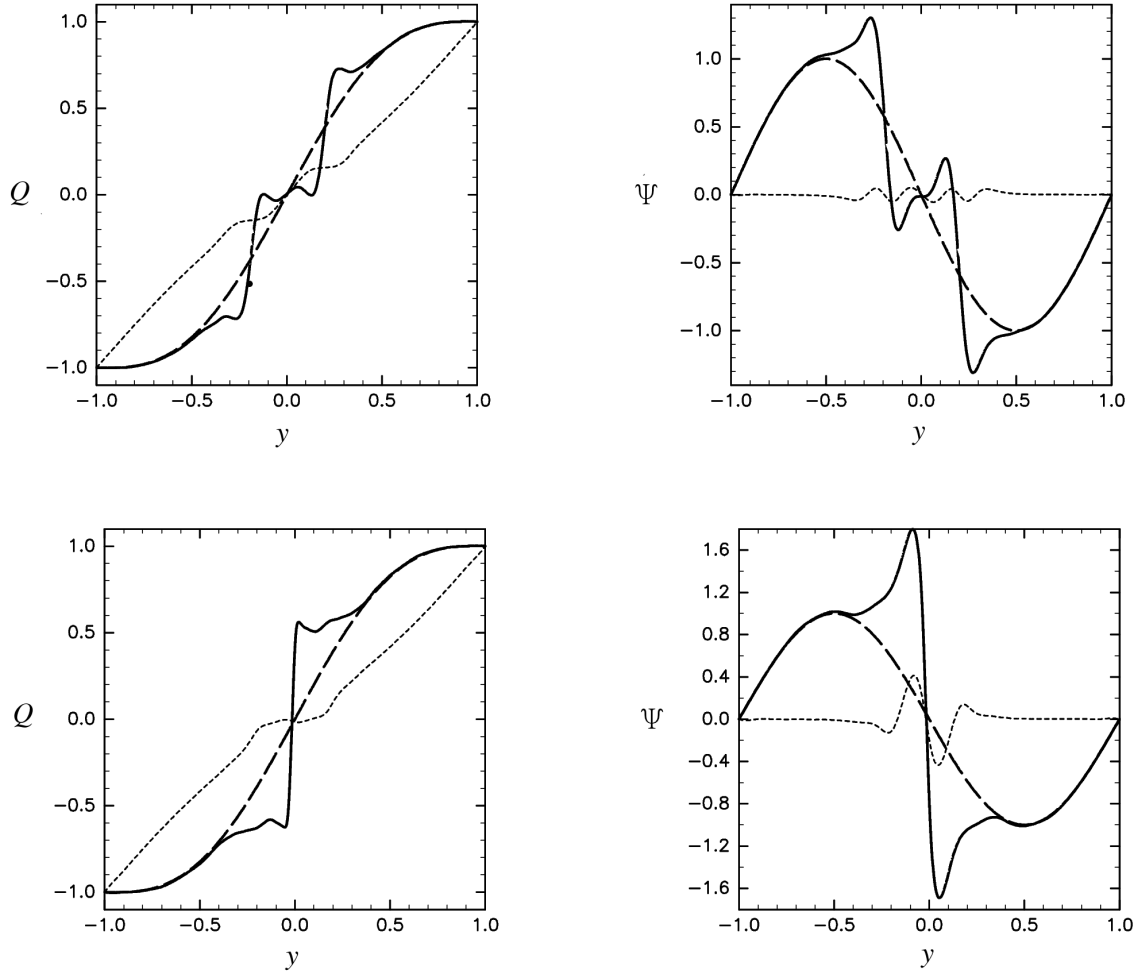


Figure 7: Meridional profiles of mean potential vorticity (left) and streamfunction (right) for $\delta_M = 0.30$ and $\delta_I = 0.9$, for $\delta_M = 0.22$ (upper) and $\delta_I = 0.9$ (lower). The solid line in the upper layer, the dotted line in the lower layer and the dashed line indicate the values estimated by the Sverdrup balance in the upper layer.

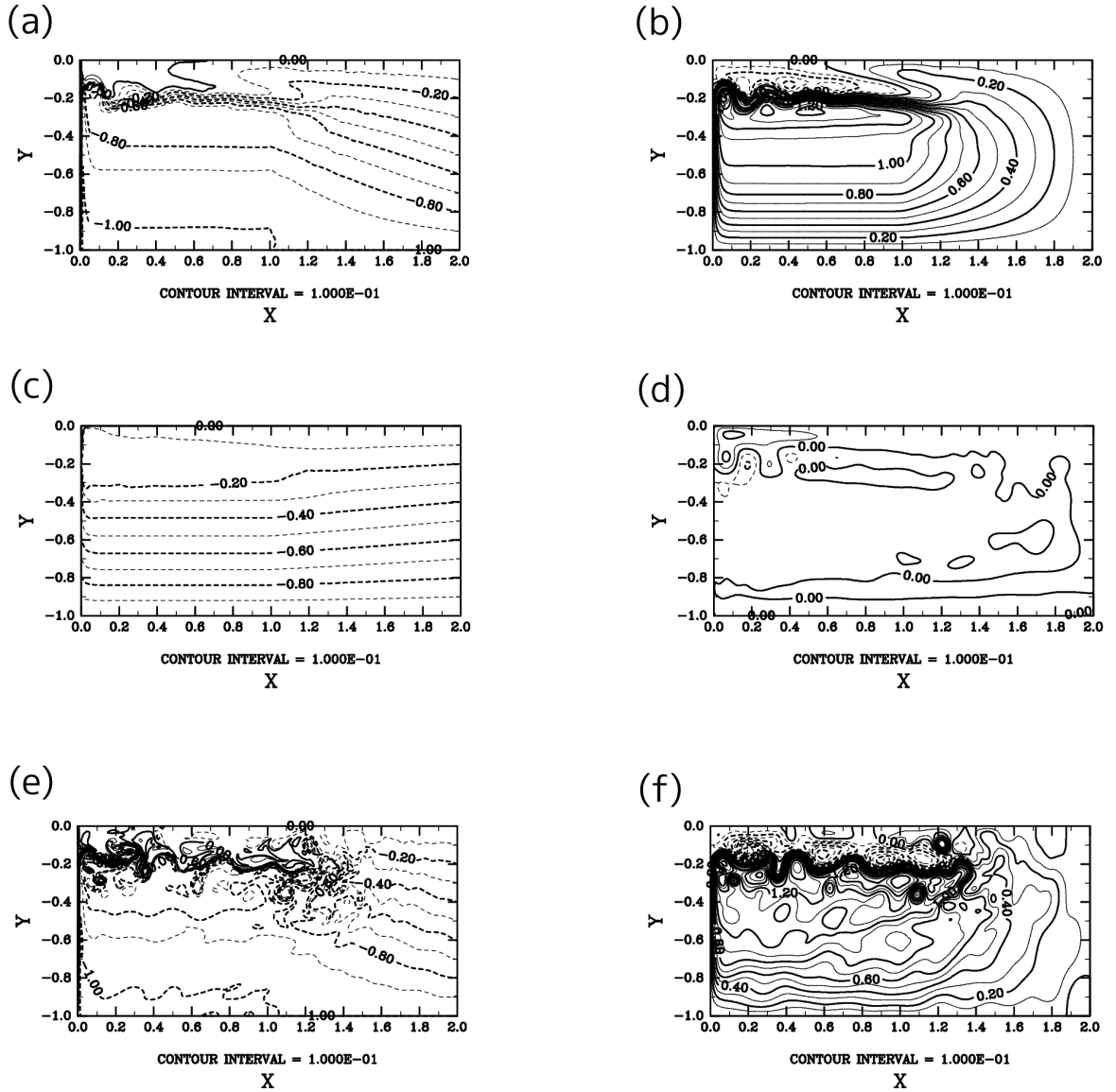


Figure 8: Typical solution of the prematurely separated jet case ($\delta_M = 0.3, \delta_I = 0.9, H_1/H_2 = 1/4$) under single-gyre forcing. (a) and (b): temporal mean fields of the upper layer potential vorticity divided by $\hat{\beta}$ and streamfunction, respectively. (c) and (d): same as (a) and (b) but for the lower layer. (e) and (f): same as (a) and (b) but for snapshots ($t=100,000$) in the upper layer.

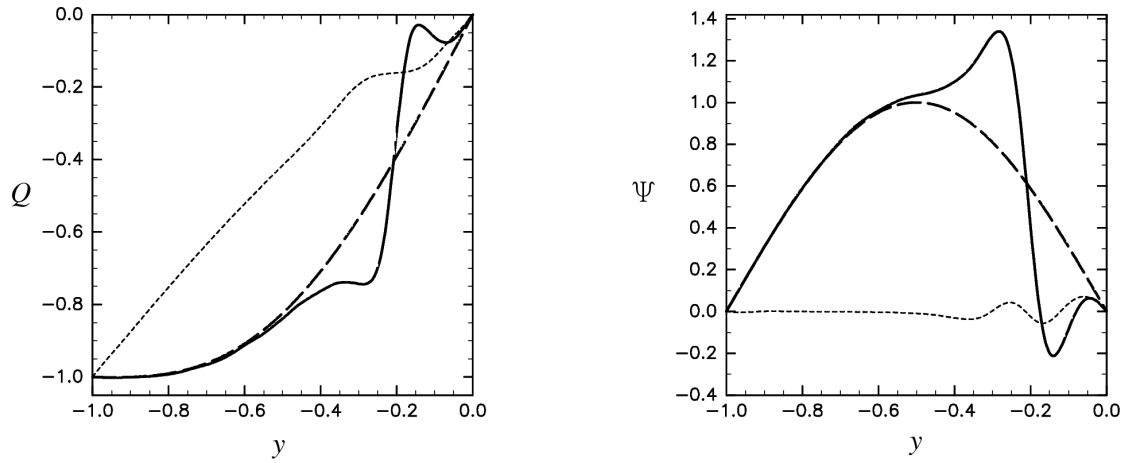


Figure 9: Meridional profiles of mean potential vorticity (left) using single-gyre forcing and streamfunction (right) for the prematurely separated jet case ($\delta_M = 0.30, \delta_I = 0.9$). Averaged from $x = 0.5$ to $x = 1.0$ in the western half region of the basin. The solid line in the upper layer, the dotted line in the lower layer and the dashed line indicate the values estimated by the Sverdrup balance in the upper layer.

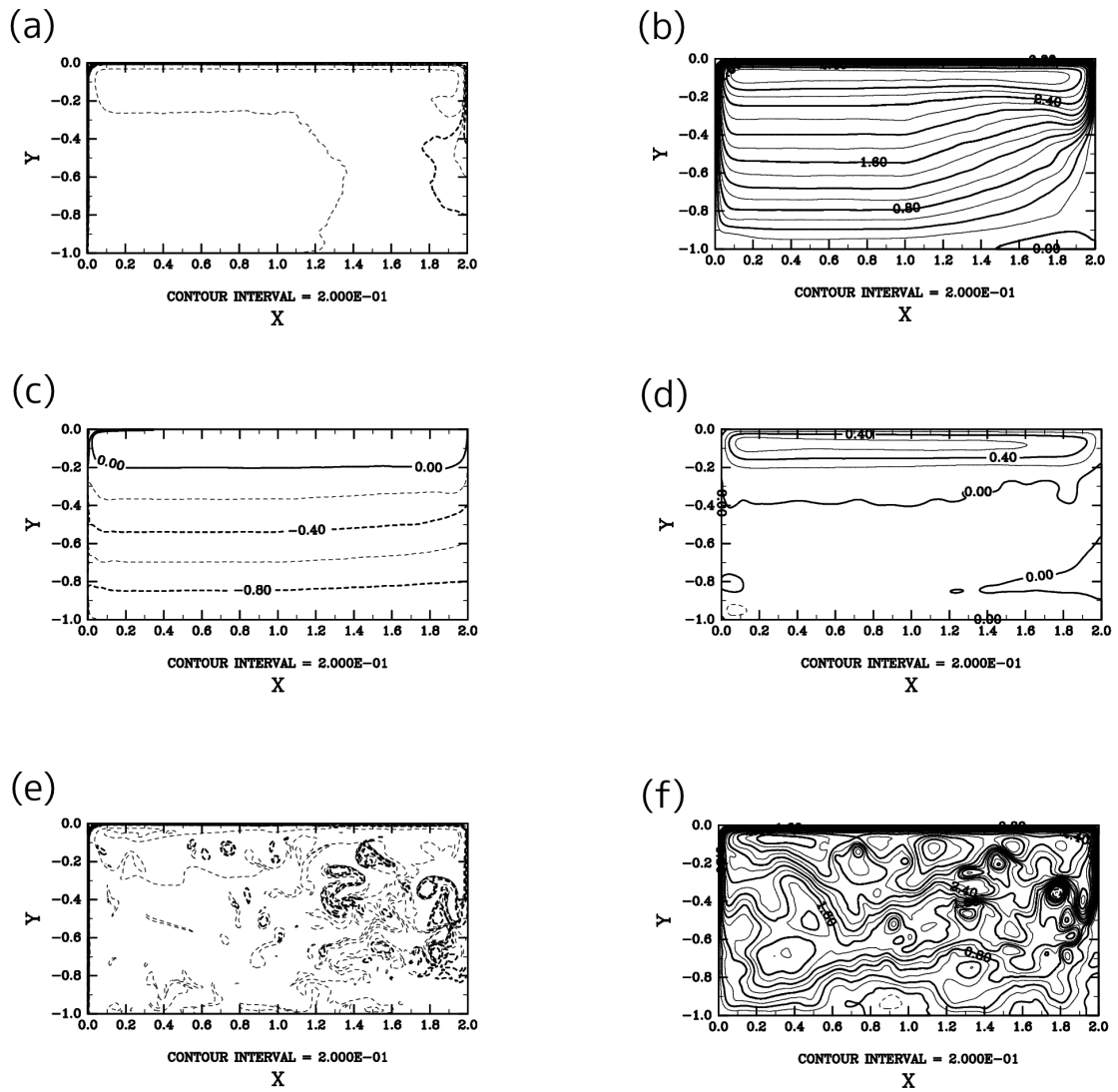


Figure 10: Same as Fig. 8 but for the gyre boundary jet case ($\delta_m = 0.22, \delta_I = 0.9$).

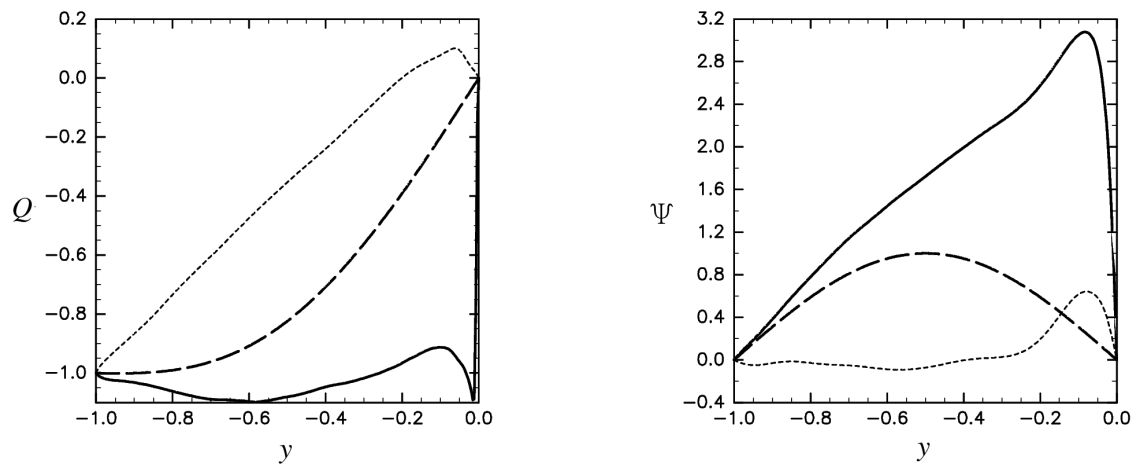


Figure 11: Same as Fig. 9 but for the gyre boundary jet case ($\delta_m = 0.22$, $\delta_I = 0.9$).

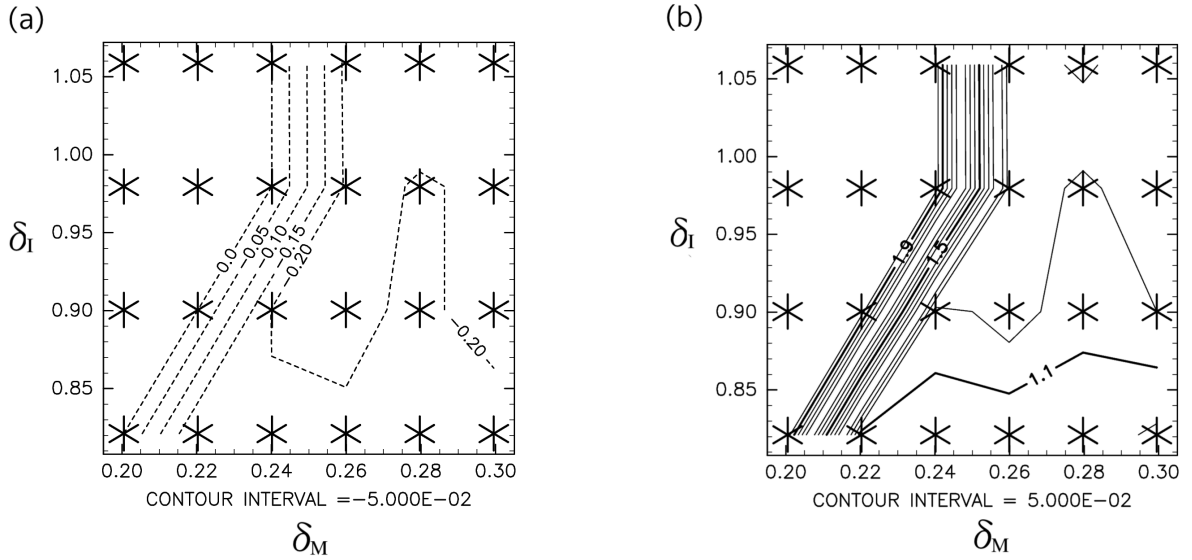
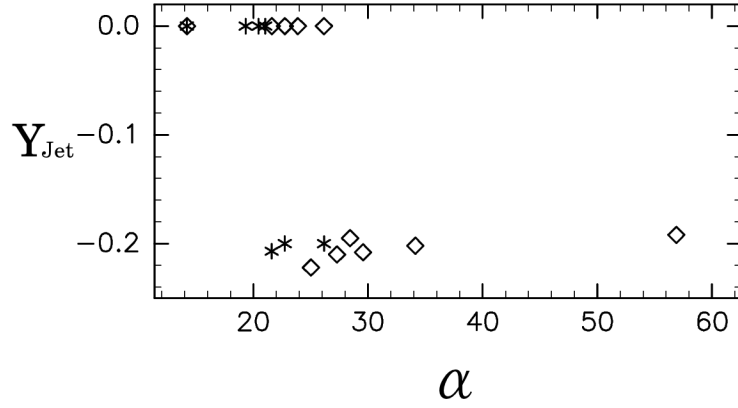


Figure 12: (a) Dependence of the y coordinate of the eastward extension jet, Y_{Jet} , on δ_M and δ_I . (b) Dependence of the jet length on δ_M and δ_I . The asterisks denote data points for which computations were made. Y_{Jet} changes discontinuously from 0 (gyre boundary jet case) to -0.2 (prematurely separated jet case) between two adjacent computational points and there is no intermediate value of Y_{Jet} . All experiments were run from rest. The final state depends on the initial condition; in many cases an initial condition in the gyre or prematurely separated jet case will persist even under parameter values in which the other state is found when spun up from rest (see text for details).

(a)



(b)

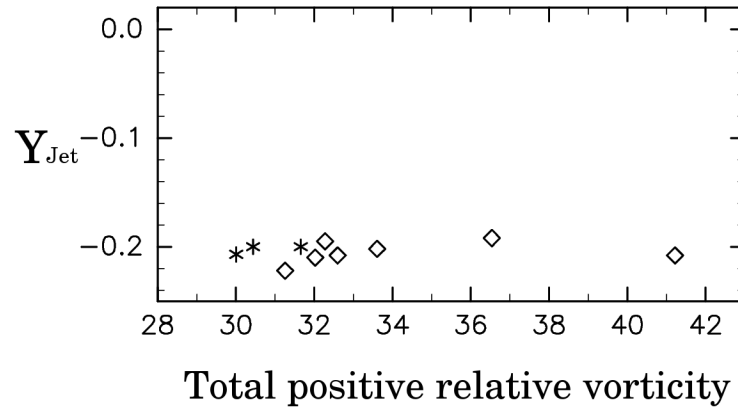


Figure 13: The y -coordinate of the extension jet, Y_{Jet} . (a) as a function of the partial-slip coefficient, α , and (b) as a function of total positive relative vorticity in western boundary layer, which is the maximum meridional velocity minus the velocity at the western boundary along $y = -0.5$. Symbols denote the data points where \diamond denote that experiments were run from the rest and * from the mean solution with prematurely separated jet under the no-slip western boundary condition. In (b), the plots are made only for the prematurely separated jet case, and the total positive vorticity is much larger for the gyre boundary jet case.

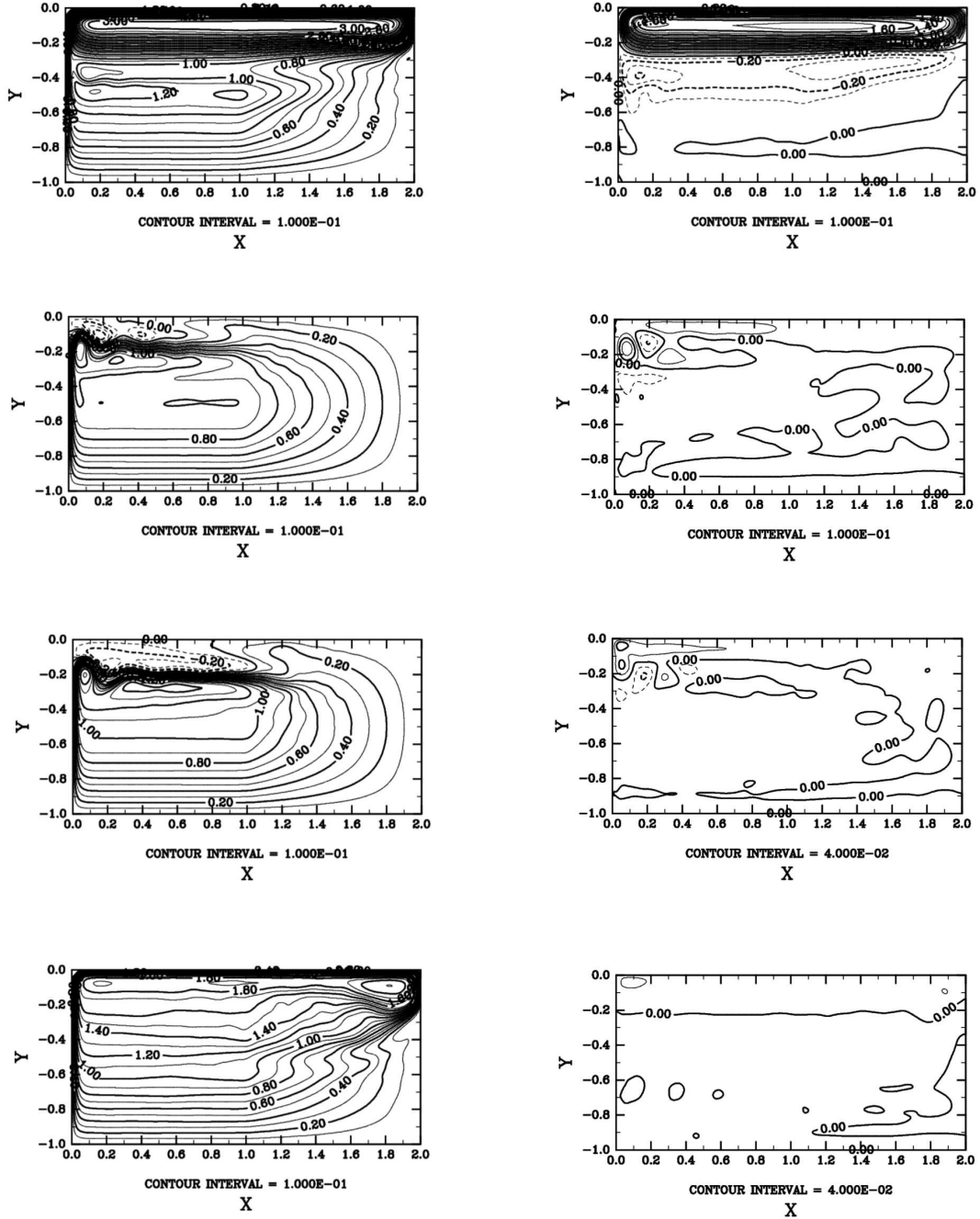


Figure 14: Time mean streamfunction field for each layer thickness ratio. $H_1/H_2 = 1/1$, $H_1/H_2 = 1/2$, $H_1/H_2 = 1/8$, $H_1/H_2 = 1/16$ from top to bottom, respectively, other parameters are as in Fig. 8. The left side shows the upper layer; the right side shows the lower layer. The contour interval is 0.4 for the last two panels on the right side and 0.1 for the others.

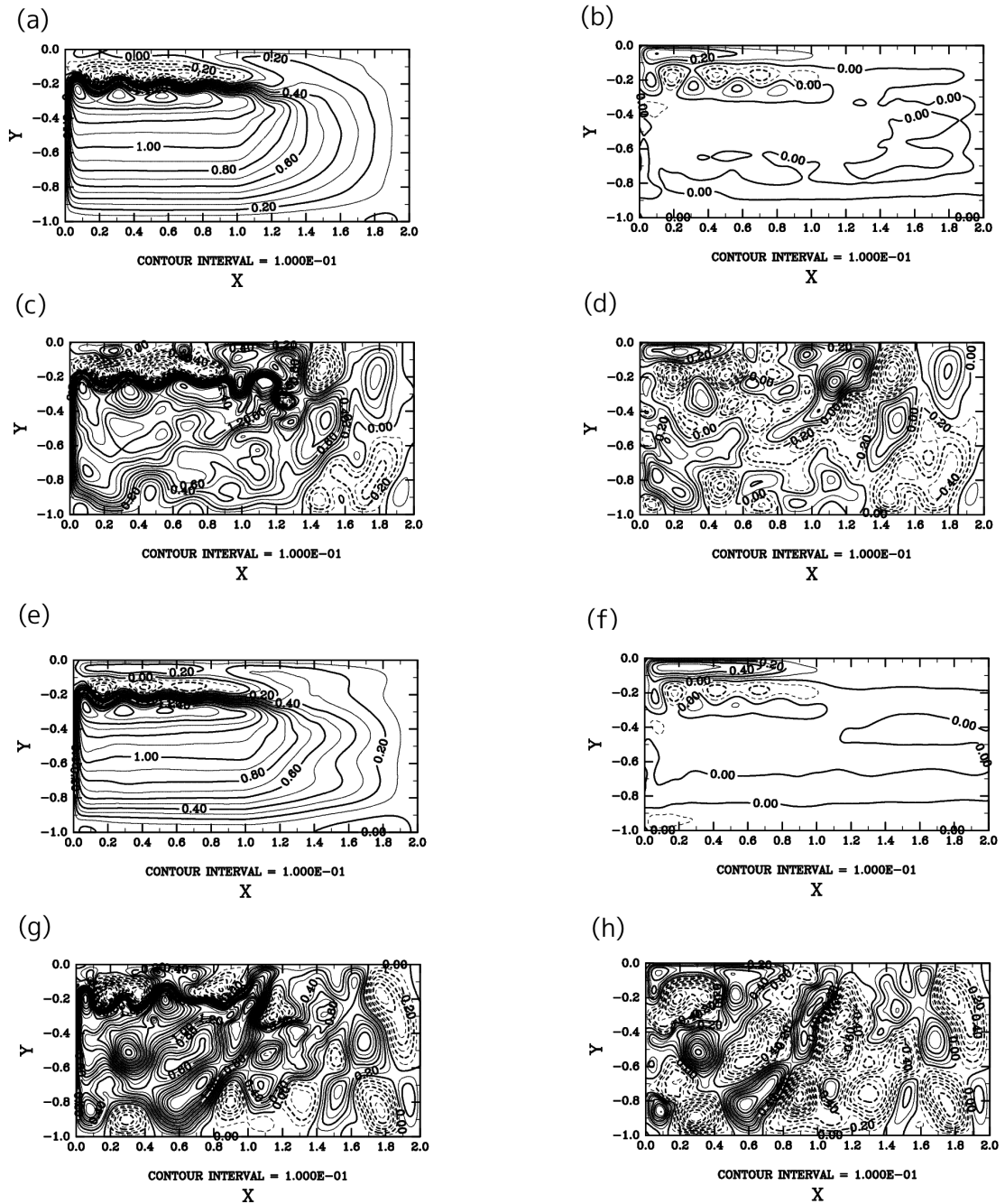


Figure 15: Streamfunction field for each coefficient of bottom friction, $\hat{\tau}$. (a) and (b): temporal mean for $\hat{\tau} = 10^{-4}$; (c) and (d): snapshot for $\hat{\tau} = 10^{-4}$; (e) and (f): temporal mean for $\hat{\tau} = 0$; (g) and (h): snapshot for $\hat{\tau} = 0$. The left side shows the upper layer, and the right side shows the lower layer.

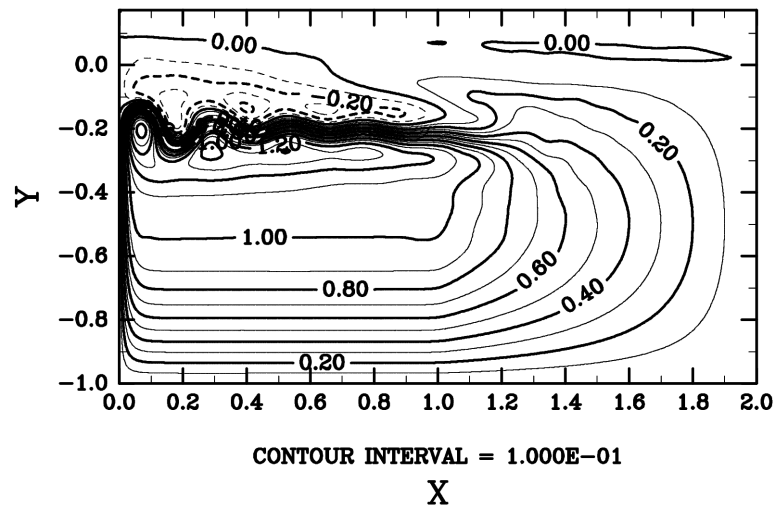
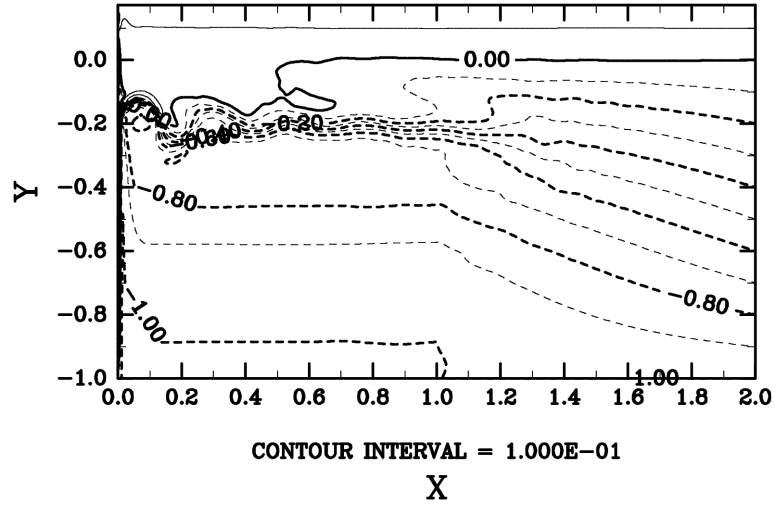


Figure 16: Result for asymmetric \hat{w}_e in the meridional direction about $y = 0$. The northern boundary is located at $Y_N = 0.2$ and $\hat{w}_e = 0$ for $y > 0$ and $\hat{w}_e = \sin(\pi y)$ for $-1.0 \leq y \leq 0$. (Upper) temporal mean potential vorticity field divided by $\hat{\beta}$; (Lower) temporal mean streamfunction field. $\delta_M = 0.30, \delta_I = 0.9$ other parameters are as in Fig. 8. A solution of the gyre boundary separation case was given as the initial condition.

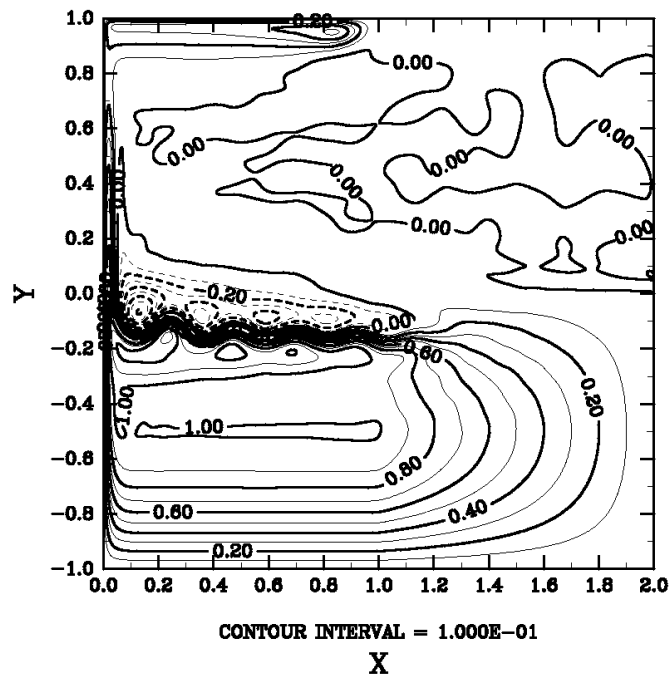
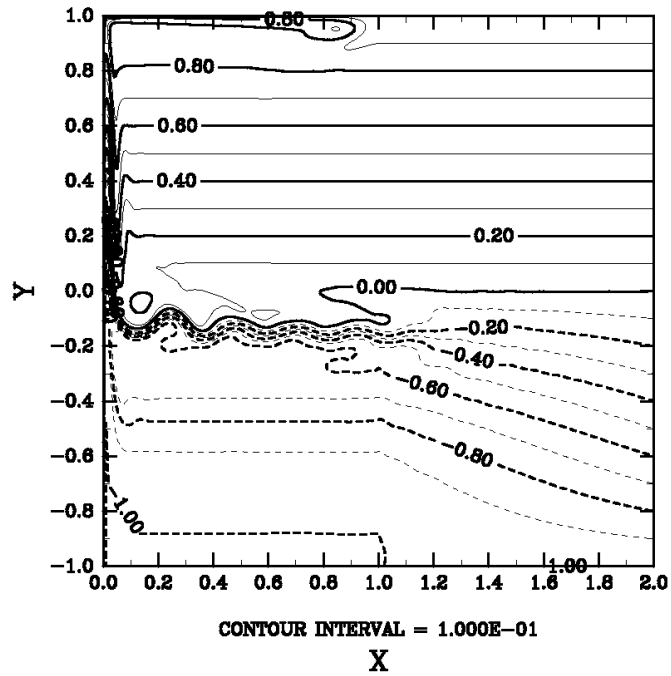


Figure 17: Same as Fig. 16 but for $Y_N = 1$ and slip western boundary condition was used.

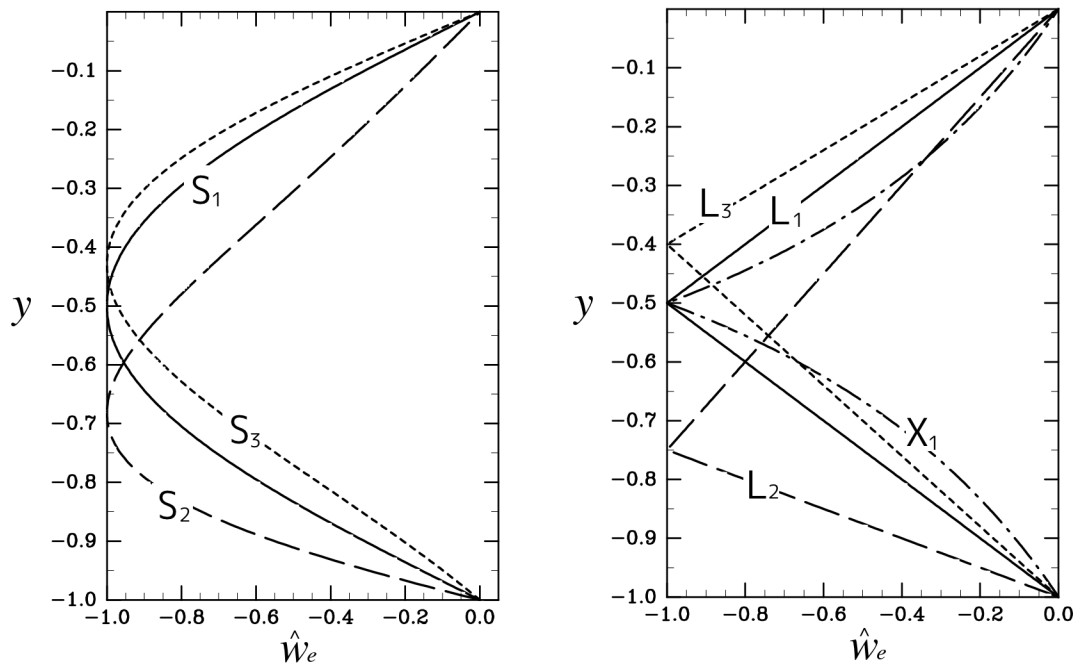


Figure 18: The meridional distribution of the Ekman pumping velocity, \hat{w}_e . The horizontal axis represents the Ekman pumping velocity. For definitions of the symbols, see Table 3.

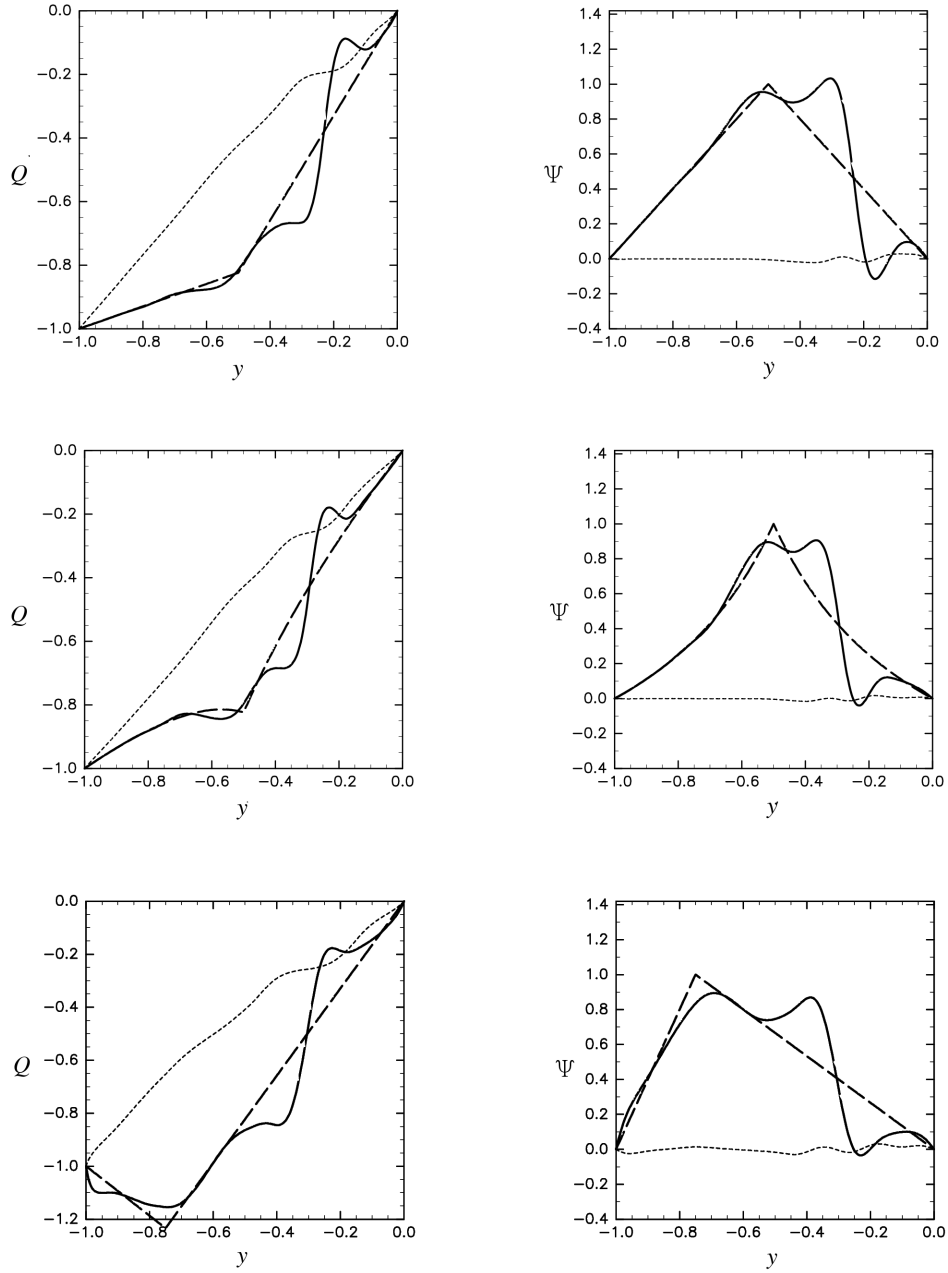


Figure 19: Meridional distribution of the temporal mean potential vorticity and streamfunction; definitions are the same as in Fig. 7. (Upper): L_1 ; (middle): X_1 ; (lower): L_2 . (Left): potential vorticity; (right): streamfunction in the upper layer (solid line) and the lower layer (dotted line) averaged in the zonal direction from $x = 0.5$ to $x = 1.0$. The dashed lines are \hat{q}_{Sv} and $\hat{\psi}_{Sv}$, which were estimated from the Sverdrup balance for the upper layer.

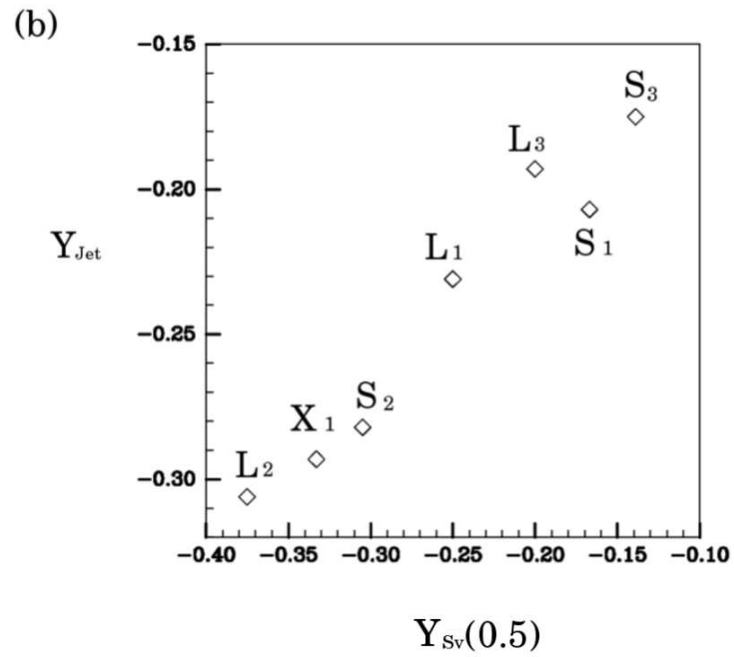
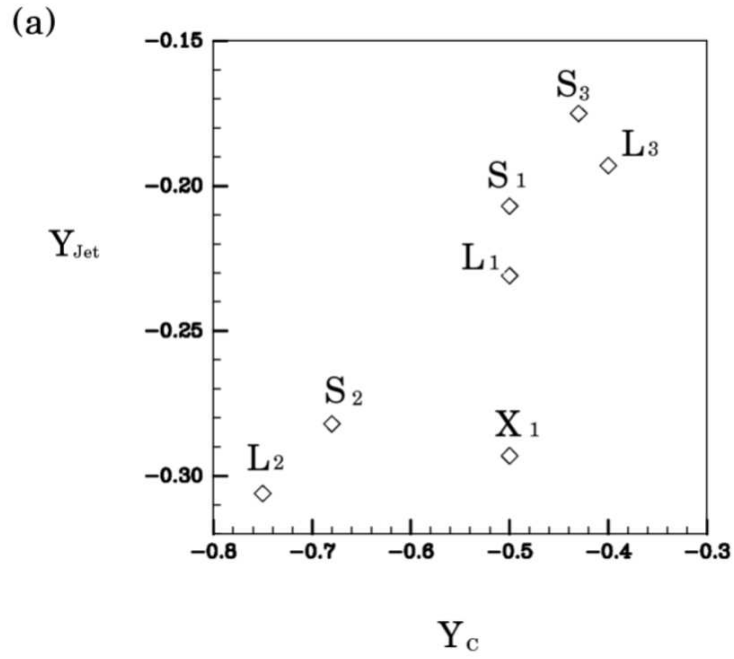
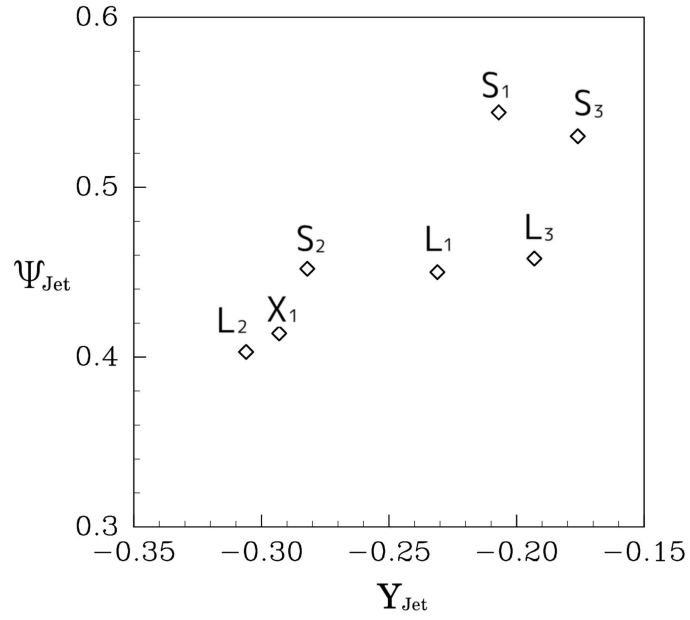


Figure 20: (a) The y -coordinate of the extension jet, Y_{Jet} , as a function of the y -coordinate of the center of the Sverdrup circulation, Y_C . (b) Y_{Jet} as a function of the y -coordinate at which $\hat{\psi}_{Sv} = 0.5$, $Y_{Sv}(0.5)$. The letter symbols in the figure correspond to Table 3. The letter symbols in the figure correspond to Table 3.

(a)



(b)

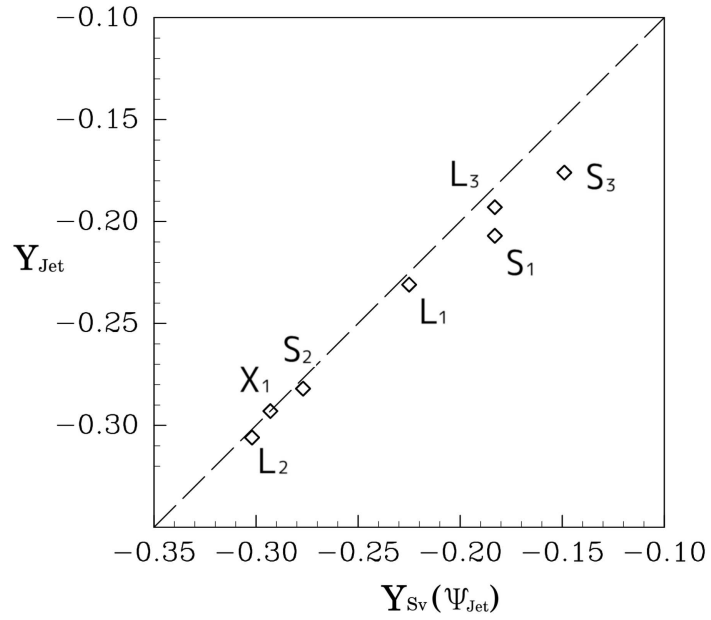


Figure 21: (a) The value of the streamfunction at the axis of the jet, Ψ_{Jet} , as a function of the y -coordinate of the extension jet, Y_{Jet} . (b) Y_{Jet} as a function of the y -coordinate at which $\hat{\psi}_{Sv} = \Psi_{Jet}$, $Y_{Sv}(\Psi_{Jet})$. The dashed line shows $Y_{Jet} = Y_{Sv}(\Psi_{Jet})$.

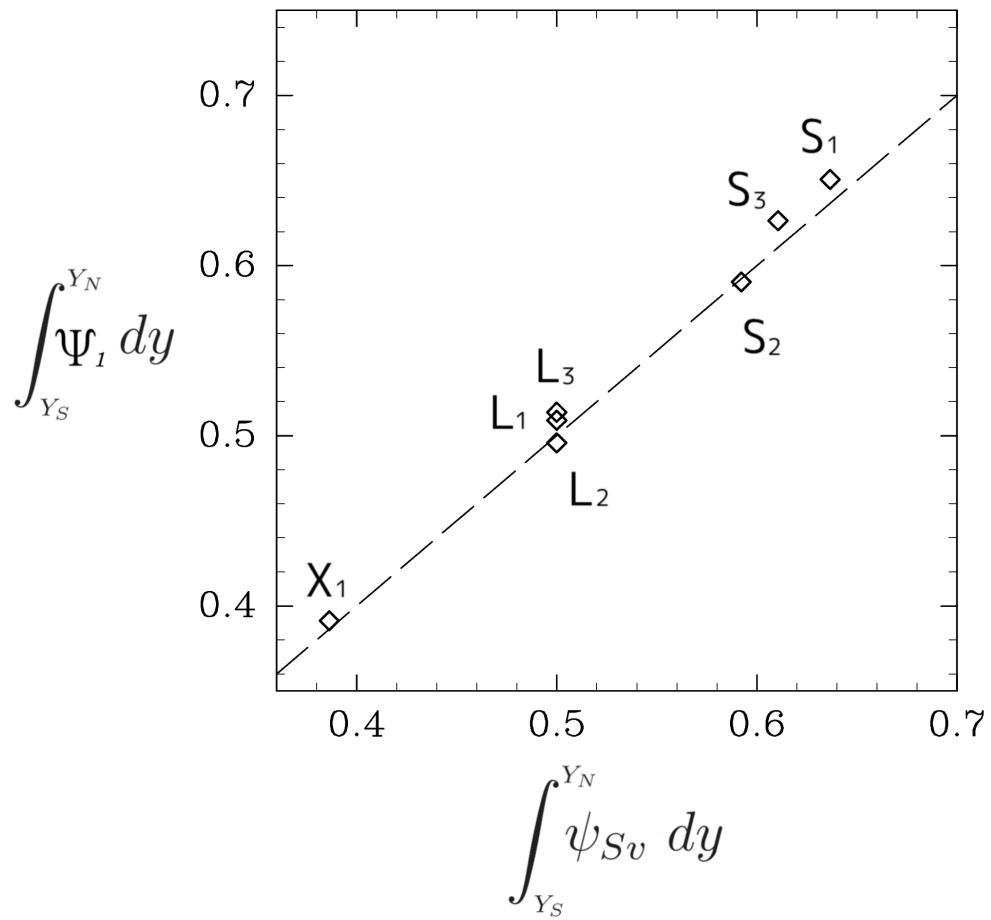


Figure 22: A plot of meridionally integrated value of time mean streamfunction against that of the Sverdrup streamfunction at arbitrary longitude in the west-half region. The dashed line shows $\int \psi_{Sv} dy = \int \Psi_1 dy$.

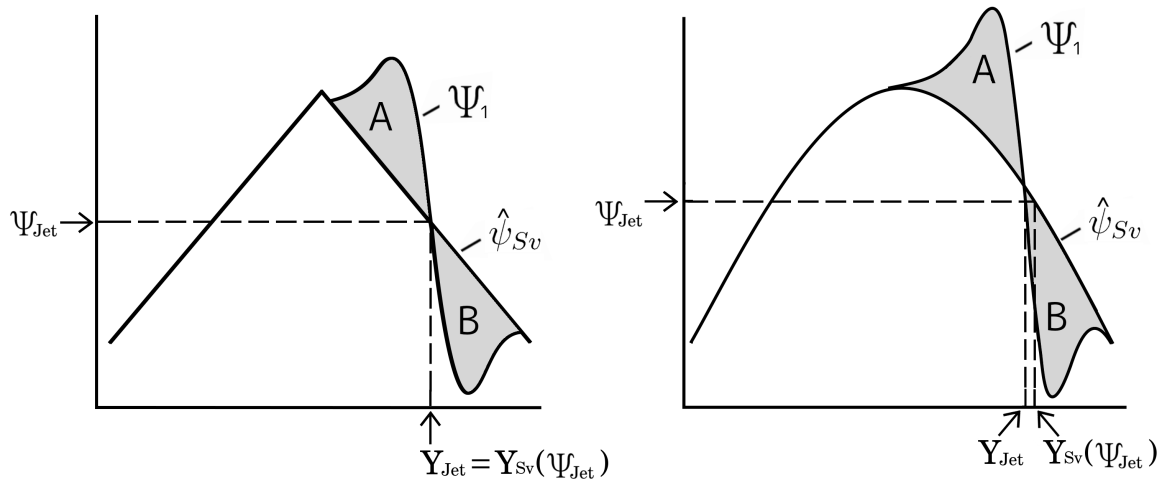


Figure 23: Schematic illustration of the change in meridional direction of Y_{Jet} arising from the change in $\hat{\psi}_{Sv}$ distribution. The area of the shadow denoted by A is equal to that by B when equation (3.5) is maintained. Because Ψ_{Jet} takes the middle value of the local maximum value and local minimum value of Ψ_1 , $Y_{Sv}(\Psi_{Jet})$ should correspond to Y_{Jet} in the case of $\frac{\partial^2 \hat{\psi}_{Sv}}{\partial y^2} = 0$, (left panel) and $Y_{Sv}(\Psi_{Jet})$ should be to the north from Y_{Jet} in the case of $\frac{\partial^2 \hat{\psi}_{Sv}}{\partial y^2} < 0$ (right panel).

Tables

Table 1: Dimensional parameters

Parameter	Meaning	Values or definition
ρ_0	density of the upper layer	1000 [kg m ⁻³]
$\Delta\rho$	density difference between the two layers	2 [kg m ⁻³]
g	gravitational acceleration	9.8 [m s ⁻²]
f	Coriolis frequency	$f_0 + \beta y$
f_0	Coriolis frequency at the reference latitude	8.3×10^{-5} [s ⁻¹]
β	meridional gradient of f	2×10^{-11} [m ⁻¹ s ⁻¹]
H_j	thickness of the j th layer	$(H_1, H_2) \approx (1000, 4000)$ [m]
H_0	whole layer thickness	$H_0 = H_1 + H_2$
W_e	Ekman pumping velocity scale	$U = f_0 W_e / \beta H_1$
R_I	Rossby radius of deformation	$\sqrt{\frac{\Delta\rho g H_1 H_2}{\rho_0 f_0^2 (H_1 + H_2)}} \approx 45$ [km]
L	meridional basin scale	$F_I^{1/2} R_I \approx 2025$ [km]
U	velocity scale of the Sverdrup flow	$U = f_0 W_e / \beta H_1$
T	time scale	$1/\beta L \approx 0.29$ [day]
ν	coefficient of horizontal viscosity	≈ 50 [m ² s ⁻¹]
r	coefficient of bottom Ekman friction	$\approx 4.0 \times 10^{-8}$ [s ⁻¹]
$\Delta x, \Delta y$	grid size	$L/256 \approx 8.0$ [km]

Table 2: Non-dimensional parameters

Parameter	Meaning	Values or definition
$F_I^{1/2} = L/R_I$	lateral basin scale in units of R_I	45 , 30
$\delta_M = (\nu/\beta)^{1/3} R_I^{-1}$	viscous WBC width in units of R_I	0.2,0.22,0.24,0.26,0.28, 0.3
$\delta_I = \sqrt{2U/\beta} R_I^{-1}$	inertial WBC width in units of R_I	0.82, 0.9 ,0.98,1.06
α	partial slip coefficient in units of $1/R_I$	from 1.4×10 to 5.7×10^2
$\frac{H_1}{H_2}$	ratio of 1st to 2nd layer thickness	$\frac{1}{1}, \frac{1}{2}, \frac{1}{4}, \frac{1}{8}, \frac{1}{16}$
$\hat{r} = r/\beta L$	coefficient of bottom friction	0, 10^{-4} , 10^{-3} , 10^{-2}
$\hat{\beta}$	non-dimensional beta	$2F_I/\delta_I^2$
$\hat{\nu}$	coefficient of horizontal viscosity	$\delta_M^3/F_I^{3/2}$

Table 3: Meridional distributions of given Ekman pumping velocities with summarized results

	Meridional distribution of $\hat{w}_e(y)$	Y_C	$y _{\psi_{Sv}=0.5}$	Y_{Jet}	$Y_{Sv}(\Psi_{Jet})$
S_1	$\hat{w}_e(y) = \sin \pi y$	-0.5	-0.167	-0.207	-0.183
S_2	$\hat{w}_e(y) = \sin \pi \{(1 - a)y + ay^3\}$ $a = 0.5$	-0.68	-0.305	-0.282	-0.277
S_3	$\hat{w}_e(y) = \sin \pi \{(1 - a)y + ay^3\}$ $a = -0.2$	-0.43	-0.140	-0.176	-0.149
L_1	$\hat{w}_e(y) = \begin{cases} 2y & (y \geq -\frac{1}{2}) \\ -2(y + 1) & (y < -\frac{1}{2}) \end{cases}$	-0.5	-0.250	-0.231	-0.225
L_2	$\hat{w}_e(y) = \begin{cases} \frac{4y}{3} & (y \geq -\frac{3}{4}) \\ -4(y + 1) & (y < -\frac{3}{4}) \end{cases}$	-0.75	-0.375	-0.306	-0.302
L_3	$\hat{w}_e(y) = \begin{cases} \frac{5y}{2} & (y \geq -\frac{2}{5}) \\ -\frac{5(y + 1)}{3} & (y < -\frac{2}{5}) \end{cases}$	-0.4	-0.200	-0.193	-0.183
X_1	$\hat{w}_e(y) = \begin{cases} \frac{y}{(1 + y)} & (y \geq -\frac{1}{2}) \\ \frac{(1 + y)}{y} & (y < -\frac{1}{2}) \end{cases}$	-0.5	-0.333	-0.293	-0.293

Bibliography

- Berloff, P. and S. Meacham, 1998: The dynamics of a simple baroclinic model of the wind-driven circulation. *J. Phys. Oceanogr.*, **28**, 2607–2634.
- Berloff, P. S. and J. C. McWilliams, 1999: Quasigeostrophic dynamics of the western boundary current. *J. Phys. Oceanogr.*, **29**, 2607–2634.
- Berloff, P. S. and J. C. McWilliams, 2002: Material transport in oceanic gyres. Part 1: Phenomenology. *J. Phys. Oceanogr.*, **32**, 764–796.
- Bleck, R., S. Dean, M. O’Keefe, and A. Sawdey, 1995: A comparison of data-parallel and message-passing versions of the Miami isopycnic coordinate ocean model. *Parallel Comput.*, **21**, 1695–1720.
- Bryan, K. and M. D. Cox, 1972: The circulation of the world ocean: A numerical study. Part I, a homogeneous model. *J. Phys. Oceanogr.*, **2**, 319–335.
- Cessi, P. and G. R. Ierley, 1995: Symmetry-breaking multiple equilibria in quasi-geostrophic, wind-driven flows. *J. Phys. Oceanogr.*, **25**, 1196–1205.
- Dengg, J., 1993: The problem of Gulf Stream separation: A barotropic approach. *J. Phys. Oceanogr.*, **23**, 2182–2200.
- Esler, J. G., 2008: The turbulent equilibration of an unstable baroclinic jet. *J. Fluid Mec.*, **599**, 241–268.

- Fox-Kemper, B., 2005: Reevaluating the roles of eddies in multiple barotropic wind-driven gyres. *J. Phys. Oceanogr.*, **35**, 1263–1278.
- Frankignoul, C., N. Sennéchal, Y.-O. Kwon, and M. A. Alexander, 2011: Influence of the meridional shifts of the Kuroshio and the Oyashio Extensions on the atmospheric circulation. *J. Climate*, **24**, 762–777.
- Griffiths, R. W. and A. E. Kiss, 1999: Flow regimes in a wide ‘sliced-cylinder’ model of homogeneous beta-plane circulation. *J. Fluid Mech.*, **399**, 205–236.
- Haidvogel, D. B., J. C. McWilliams, and P. R. Gent, 1992: Boundary current separation in a quasigeostrophic eddy-resolving ocean model. *J. Phys. Oceanogr.*, **22**, 882–902.
- Han, Y. J., 1984: A numerical world ocean general circulation model Part 2. a baroclinic experiment. *Dyn. Atmos. Oceans*, **8**, 141–172.
- Ibrayev, R. A., R. N. Khabeev, and K. V. Ushakov, 2012: Eddy resolving $1/10^\circ$ model of the world ocean. *Izvestiya Atmos. Ocean. Phys.*, **48**, 37–46.
- Ierley, G. R., 1987: On the onset of inertial recirculation in barotropic general circulation models. *J. Phys. Oceanogr.*, **17**, 2366–2374.
- Ierley, G. R., 1990: Boundary layers in the general ocean circulation. *Ann. Rev. Fluid Mech.*, **22**, 111–142.
- Ierley, G. R. and O. G. Ruehr, 1986: Analytic and numerical solutions of a nonlinear boundary-layer problem. *Stud. Appl. Math.*, **75**, 1–36.
- Ierley, G. R. and V. A. Sheremet, 1995: Multiple solutions and advection-dominated flow in the wind-driven circulation. Part 1: Slip. *J. Mar. Res.*, **53**, 703–737.
- Imai, Y., T. Aoki, and K. Takizawa, 2008: Conservative form of interpolated differential

- operator scheme for compressible and incompressible fluid dynamics. *J. Comput. Phys.*, **227**, 2263–2285.
- Jiang, S., F. Jin, and M. Ghil, 1995: Multiple equilibria, periodic, and aperiodic solutions in a wind-driven double-gyre, shallow-water model. *J. Phys. Oceanogr.*, **25**, 764–786.
- Kamenkovich, V. M., V. A. Sheremet, A. R. Pastushkov, and S. O. Belotserkovsky, 1995: Analysis of the barotropic model of the subtropical gyre in the ocean for finite Reynolds numbers. Part 1. *J. Mar. Res.*, **53**, 959–994.
- Kiss, A. E., 2002: Potential vorticity “crises”, adverse pressure gradients, and western boundary current separation. *J. Mar. Res.*, **60**, 779–803.
- Marshall, D. P. and D. P. Tansley, 2001: An implicit formula for boundary current separation. *J. Phys. Oceanogr.*, **31**, 1633–1038.
- Masumoto, Y., et al., 2004: A fifty-year eddy-resolving simulation of the world ocean preliminary outcomes of ofes (ogcm for the earth simulator). *J. Earth Sim.*, **1**, 35–56.
- McCalpin, J. D. and D. B. Haidvogel, 1996: Phenomenology of the low-frequency variability in a reduced-gravity, quasigeostrophic double-gyre model. *J. Phys. Oceanogr.*, **26**, 739–752.
- McWilliams, J. C., 1996: Modeling the oceanic general circulation. *Ann. Rev. Fluid. Mech.*, **28**, 215–248.
- Milliff, R. F., J. Morzel, D. B. Chelton, and M. H. Freilich, 2004: Wind stress curl and wind stress divergence biases from rain effects on QSCAT surface wind retrievals. *J. Atmos. Ocean. Technol.*, **21**, 1216–1231.
- Munk, W., 1950: On the wind-driven ocean circulation. *J. Meteor.*, **7**, 79–93.

- Nakano, H., H. Tsujino, and R. Furue, 2008: The Kuroshio Current system as a jet and twin “relative” recirculation gyres embedded in the Sverdrup circulation. *Dyn. Atmos. Oceans*, **45**, 135–164.
- Özgökmen, T. M., E. P. Chassignet, and A. M. Paiva, 1997: Impact of wind forcing, bottom topography, and inertia on midlatitude jet separation in a quasigeostrophic model. *J. Phys. Oceanogr.*, **27**, 2460–2476.
- Pedlosky, J., 1987: *Geophysical Fluid Dynamics*. Springer, New York, 710 pp.
- Pedlosky, J., 1996: *Ocean Circulation Theory*. Springer, New York, 453 pp.
- Pierini, S., 2006: A Kuroshio Extension system model study: Decadal chaotic self-sustained oscillations. *J. Phys. Oceanogr.*, **36**, 1605–1625.
- Primeau, F. W. and D. Newman, 2007: Bifurcation structure of a wind-driven shallow water model with layer-outcropping. *Ocean Model.*, **36**, 250–263.
- Sasai, C. Y., K. J. Richards, A. Ishida, and H. Sasaki, 2010: Effects of cyclonic mesoscale eddies on the marine ecosystem in the Kuroshio Extension region using an eddy-resolving coupled physical-biological model. *Ocean Dynamics*, **60**, 693–704.
- Sasaki, Y. N. and N. Schneider, 2011: Decadal shifts of the Kuroshio Extension Jet: Application of thin-jet theory. *J. Phys. Oceanogr.*, **41**, 979–993.
- Smith, R. D., M. E. Maltrud, F. O. Bryan, and M. W. Hecht, 2000: Numerical simulation of the North Atlantic Ocean $\frac{1}{10}^\circ$. *J. Phys. Oceanogr.*, **30**, 1532–1561.
- Stommel, H., 1948: The westward intensification of wind-driven ocean currents. *Trans. Am. Geophys. Union.*, **29**, 202–206.
- Sugimoto, S. and K. Hanawa, 2012: Relationship between the path of the Kuroshio in

- the south of Japan and the path of the Kuroshio Extension in the east. *J. Oceanogr.*, **68**, 219–225.
- Takano, K., Y. Mintz, and Y. Han, 1973: Numerical simulation of world ocean circulation. *Bull. Amer. Meteor. Soc.*, **54**, 749–749.
- Trenberth, K. E. and J. M. Caron, 2001: Estimates of meridional atmosphere and ocean heat transports. *J. Climate*, **14**, 3433–3443.
- Vallis, G. K., 2006: *Atmospheric and Oceanic Fluid Dynamics*. Cambridge Univ. Press, New York, 745 pp.
- Verron, J. and E. Blayo, 1996: The no-slip condition and separation of western boundary currents. *J. Phys. Oceanogr.*, **26**, 1938–1951.
- Verron, J. and J. H. Jo, 1994: On the stability of wind-driven barotropic ocean circulations. *Fluid Dyn. Res.*, **14**, 7–27.
- Verron, J. and C. Le Provost, 1991: Response of eddy-resolved general circulation numerical models to asymmetrical wind forcing. *Dyn. Atmos. Oceans*, **15**, 505–533.